MASTERARBEIT | MASTER'S THESIS

Titel | Title

ALMA observations in the Orion Molecular Cloud 2

verfasst von | submitted by

Lukas Orion BSc

angestrebter akademischer Grad | in partial fulfilment of the requirements for the degree of

Master of Science (MSc)

Wien | Vienna, 2025

Studienkennzahl lt. Studienblatt | Degree programme code as it appears on the student record sheet:	UA 066 861
Studienrichtung lt. Studienblatt | Degree programme as it appears on the student record sheet:	Masterstudium Astronomie
Betreut von | Supervisor:	Assoz. Prof. Dr. Alvaro Hacar Gonzalez MA

Acknowledgements

The author, Lukas Orion (LO), thanks the thesis supervisor Assoc.Prof. Dr. Álvaro Hacar for all the suggestions, comments, and discussions that helped improve the quality of the thesis. LO also thanks Andrea Socci and Francesca Bonanomi for their insightful discussions and comments. Moreover, LO thanks Eelco van Kampen for the calibration of the visibilities of the 2016.1.00681.S project. This project made use of the following ALMA data (project codes): 2015.1.00669.S, 2016.1.00681.S, 2016.1.00376.S, and 2017.1.01353. ALMA is a partnership of ESO (representing its member states), NSF (USA) and NINS (Japan), together with NRC (Canada), NSTC and ASIAA (Taiwan), and KASI (Republic of Korea), in cooperation with the Republic of Chile. This research made use of NumPy (Harris et al. 2020), SciPy (Virtanen et al. 2020), Astropy (Collaboration et al. 2022), Matplotlib (Hunter 2007), Pandas (pandas development team 2020) and ALminer (Ahmadi & Hacar 2023) inside of a Python environment in Visual Studio Code. This project made use of the CASA (CASA Team et al. 2022), CLASS[1] and TOPCAT (Taylor 2005) software. All interferometry concepts (Chapter 4) were taken from the ALMA Cycle 10 Technical Handbook (Cortes et al. 2023). This work made use of ChatGPT for code debugging in Python to improve the quality of the code. This work made use of Overleaf's Writefull software to improve the quality of the text.

[1] http://www.iram.fr/IRAMFR/GILDAS

Abstract

The Orion Molecular Cloud 2 (OMC-2) region is one of the most active star formation regions in the solar neighborhood (Peterson & Megeath 2008). Within $\sim 0.2\,\mathrm{pc}$, OMC-2 is forming more than a dozen low-mass YSOs at different evolutionary stages and includes the famous OMC-2 FIR-4 intermediate-mass object. Due to its proximity, OMC-2 is typically employed as benchmark for new kinematic, evolution, and chemistry studies (Hacar et al. 2018). OMC-2 has been extensively explored in recent years using ALMA observations in multiple bands and configurations, producing a plethora of continuum and molecular line maps at different frequencies (Hacar et al. 2018). This project will use the ALminer toolkit (Ahmadi & Hacar 2023) for the efficient extraction of the ALMA Science Archive to explore the molecular content of the OMC-2 region. When possible, we will combine these ALMA observations with previous single-dish data using advanced data combination techniques. The goal of this project is to collect the largest database of ALMA observations of this region and to produce the first panchromatic view of this region with ALMA. In particular, our main objective was to explore the gas kinematics of dense tracers such as N_2H^+, while the secondary objective was to characterize OMC-2 with other tracers such as the dust continuum, shock (CH_3OH & SiO) and outflow tracers (e.g. CO).

We combined the data of the two chosen N_2H^+ projects (see Tab. 5.1) and produced a high angular resolution (1.8″) image of OMC-2 FIR 4 thanks to the retrieved Fontani et al. (2020) project while preserving the high sensitivity of the lower resolution image of Hacar et al. (2018). The resulting dense gas structure shows multiple sub-filaments (fibers) that are connected through the central FIR 4 hub (see Fig. 6.2). Our kinematic analysis shows that more or less half of the gas is subsonic (48.9%), while the other half is transonic (35. 0%) and subsonic (16. 1%) (see Tab. 6.1). Our derived Mach numbers in OMC-2 FIR 4 range from 0.3 to 4.3 and do not correlate with high-velocity structures (see Fig. 6.4), such as the FIR 3 outflow (Osorio et al. 2017) or VLA 15 jet (Chahine et al. 2022). However, our derived column densities in OMC-2 FIR 4 correlate with the dense gas distribution, where the column densities range from $3 \times 10^{21}\,\mathrm{cm}^{-2}$ to $2 \times 10^{23}\,\mathrm{cm}^{-2}$ (see Fig. 6.5). The dust continuum map (Fontani et al. 2020) traced most of the Spitzer protostars (Furlan et al. 2016) and the bulk distribution of our N_2H^+ dense gas component (see Fig. 6.8). The shock tracer CH_3OH (Chahine et al. 2022) revealed that there is a correlation between the position of the FIR 4 clump cavities and the peak emission, while the SiO emission coincides with the distribution of the VLA 15 jet (see Fig. 6.9). The main blue-shifted and red-shifted CO emission (Sato et al. 2023) traces the bipolar molecular outflow from FIR 3, where the southern outflow impacts the FIR 4 clump (see Fig. 6.11). In addition, we created a FIR 3 molecular outflow model with a position angle of 53°, opening angle of 78°, and flow velocity of $4.5\,\mathrm{km\,s}^{-1}$ (see Fig. 6.14). Our model and the derived collisional Mach number of 14 provide a quantitative basis for interpreting the outflow as a driving mechanism for the observed structure and kinematics in OMC-2 FIR 4. This implies the presence of strong shocks that are capable of compressing the gas and potentially triggering star formation (Shimajiri et al. 2008).

Kurzfassung

Die Orion Molecular Cloud 2 (OMC-2) Region ist eine der aktivsten Sternentstehungsregionen in der solaren Nachbarschaft (Peterson & Megeath 2008). Innerhalb von 0,2 pc bildet OMC-2 mehr als ein Dutzend massearmer YSOs (Young Stellar Objects) in verschiedenen Entwicklungsstadien und beherbergt das bekannte Objekt mittlerer Masse OMC-2 FIR-4. Aufgrund ihrer Nähe wird OMC-2 typischerweise als Referenzregion für neue kinematische, evolutionäre und chemische Studien verwendet (Hacar et al. 2018). In den letzten Jahren wurde OMC-2 intensiv mit ALMA-Beobachtungen in mehreren Bändern und Konfigurationen untersucht, was zu einer Vielzahl von Kontinuums- und Moleküllinien Diagramme bei verschiedenen Frequenzen führte (Hacar et al. 2018).

Dieses Projekt verwendet das ALminer-Toolkit (Ahmadi & Hacar 2023) zur effizienten Extraktion aus dem ALMA Science Archive, um den molekularen Inhalt der OMC-2-Region zu untersuchen. Wenn möglich, werden wir diese ALMA-Beobachtungen mit früheren Einzelantennen-Daten unter Verwendung fortschrittlicher Kombinationstechniken zusammenführen. Ziel dieses Projekts ist es, die größte Datenbank von ALMA-Beobachtungen dieser Region zu sammeln und die erste panchromatische Ansicht dieser Region mit ALMA zu erstellen.

Insbesondere war unser Hauptziel die Untersuchung der Kinematik dichter gas Tracer wie N_2H^+, während das sekundäre Ziel darin bestand, OMC-2 mit anderen Tracern wie dem Staubkontinuum, Schock-Tracern (CH_3OH & SiO) und Outflow-Tracern (z.B. CO) zu charakterisieren. Wir kombinierten die Daten der beiden ausgewählten N_2H^+-Projekte (siehe Tab. 5.1) und erzeugten ein hochaufgelöstes Bild (1,8″) von OMC-2 FIR 4, dank des Projekts von Fontani et al. (2020), wobei gleichzeitig die hohe Empfindlichkeit des Bildes mit niedrigerer Auflösung von Hacar et al. (2018) erhalten blieb.

Die resultierende dichte Gasstruktur zeigt mehrere Sub-Filamente (sogenannte „fibers“), die durch das zentrale FIR-4-Hub verbunden sind (siehe Abb. 6.2). Unsere kinematische Analyse zeigt, dass etwa die Hälfte des Gases subsonisch ist (48,9%), während der Rest transsonisch (35,0%) und supersonisch (16,1%) ist (siehe Tab. 6.1). Die abgeleiteten Mach-Zahlen in OMC-2 FIR 4 reichen von 0,3 bis 4,3 und korrelieren nicht mit Hochgeschwindigkeitsstrukturen (siehe Abb. 6.4), wie dem Outflow von FIR 3 (Osorio et al. 2017) oder dem VLA 15-Jet (Chahine et al. 2022). Unsere abgeleiteten Säulendichten in OMC-2 FIR 4 hingegen korrelieren mit der Verteilung des dichten Gases, wobei die Säulendichten zwischen 3×10^{21} cm^{-2} und 2×10^{23} cm^{-2} liegen (siehe Abb. 6.5).

Das Staubkontinuums Diagramm Fontani et al. (2020) korrellierte mit die meisten Spitzer-Protosterne (Furlan et al. 2016) sowie die Hauptverteilung unserer N_2H^+-Komponente des dichten Gases (siehe Abb. 6.8). Der Schocktracer CH_3OH (Chahine et al. 2022) zeigte eine Korrelation zwischen der Position der FIR-4 Kavitäten und der maximalen Emission, während die SiO-Emission mit der Verteilung des VLA 15-Jets übereinstimmt (siehe Abb. 6.9). Die maximale blau- und rotverschobene CO-Emission (Sato et al. 2023) zeichnet den bipolaren molekularen

Outflow von FIR 3 nach, wobei der südliche Outflow auf FIR-4 trifft (siehe Abb. 6.11).

Zusätzlich erstellten wir ein Modell des molekularen Outflow von FIR 3 mit einem Positionswinkel von 53°, einem Öffnungswinkel von 78° und einer Flussgeschwindigkeit von 4,5 km/s (siehe Abb. 6.14). Unser Modell und die abgeleitete kollisionsbedingte Mach-Zahl von 14 liefern eine quantitative Grundlage für die Interpretation des Ausflusses als treibenden Mechanismus für die beobachtete Struktur und Kinematik in OMC-2 FIR 4. Dies weist auf das Vorhandensein starker Schocks hin, die in der Lage sind, das Gas zu komprimieren und möglicherweise die Sternentstehung auszulösen (Shimajiri et al. 2008).

Contents

List of Tables

List of Figures

1 Introduction

1.1 Interstellar Medium

The Interstellar Medium (ISM) is the matter and radiation that exist in the space between stars in a galaxy. It plays a crucial role in the formation and evolution of stars and serves as the raw material for star formation. The dense gas reservoirs present in the ISM are affected by cooling and then collapse into molecular clouds (nursery of stars).

The ISM consists of gas, dust, and cosmic rays. Gas makes up $\sim 99\%$ of the mass of ISM and is mainly abundant in hydrogen and helium, with small amounts of heavier elements ("metals"). After molecular hydrogen (H_2), most molecules are based on carbon, oxygen, and nitrogen. Molecular gas is found in dense and cold clouds (Molecular Clouds) with number densities ranging from $10^2\,\mathrm{cm^{-3}}$ to $10^6\,\mathrm{cm^{-3}}$ and temperatures from 10 K to 50 K. Here, molecules can form without being ionized (self-shielding). Molecular clouds have sizes ranging from $\sim 10\,\mathrm{pc} - 100\,\mathrm{pc}$.

Inside of the molecular clouds one can find filaments, which are $\sim 1\,\mathrm{pc} - 10\,\mathrm{pc}$ long and ~ 0.1 pc thick structures (André et al. 2010). Hacar et al. (2013) suggested that filaments have an intrinsic substructure made of so-called fibers. These fibers are characterized by their continuity in space and velocity, and transonic internal velocity dispersions along their typical length of ~ 0.5 pc (Hacar et al. 2013). Within the filaments, one can find spherical localized overdensities ($n_{\mathrm{H_2}} \sim 10^4\,\mathrm{cm^{-3}} - 10^6\,\mathrm{cm^{-3}}$) of size ~ 0.1 pc called cores (Könyves et al. 2010). Cores form from fragmentation of filaments. Whithin supercritical filaments above a given column density (equivalent to $A_V \sim 7$ magnitudes), cores collapse and form stars (André et al. 2014).

The stage that occurs after a dense core begins collapsing but before the star is born, and hence hydrogen fusion begins in its core, is called the protostellar stage. To determine the evolutionary state of a protostar, one needs to look at the characteristics of its spectral energy distribution (SED). Class 0 phase protostars are the youngest types of protostars and are distinguishable because of the dense infalling envelope of gas and dust that surrounds the protostar (Andre et al. 1993). The next protostar phase is called Class I, where the protostar is still surrounded by the envelope but a lot less deep embedded than in the Class 0 case. At the end of Class I most of the envelope is dissipated. A Class II object (T-Tauri star) has most of its surrounding envelope gone, leaving a protostar surrounded by a prominent protoplanetary disk. Finally, a Class III object is when the protostar transitions to a fully formed star (pre-main sequence). One of the most prominent diagnostics of protostar evolution through a SED is the bolometric temperature (Chen et al. 1995). For example, a bolometric temperature of $T_{\mathrm{bol}} = 70\,\mathrm{K}$ is found as the division between the Class 0 and Class I protostars (Dunham et al. 2014).

Dust makes up only $\sim 1\%$ of the mass of the ISM but is crucial for the ISM. It is made of silicates, carbonaceous materials, and ices. Starlight is absorbed and scattered by dust and then re-emitted in infrared (IR). This is attributed to the $\sim$ µm size of the dust grains. Dust grains are seen as catalysts for chemistry in dark clouds, since they help to form molecules by acting as surfaces for chemical reactions (e.g., formation of H_2).

1.2 Molecular emission

To study the nature of molecular clouds (star formation nurseries), astronomers observe molecular emission coming from them. Molecular emission carries information about gas thermodynamics, chemistry, column & volume densities, velocity structure, and much more (physical conditions in the ISM). Although H_2 is the most abundant molecule in the ISM, its rotational emission lines are not excitable at molecular cloud temperatures (homo-nuclear molecule). The next most abundant molecular tracer is CO (carbon monoxide). CO has rotational transitions (e.g. $J = 1-0; J = 2-1$) that are easily excitable at low molecular cloud temperatures, which make it a good tracer for the main molecular cloud structure (Peñaloza et al. 2017). Nitrogen-bearing molecules such as N_2H^+, HCN and NH_3 (ammonia) are used as tracers for dense gas in cores and filaments. This is because these molecules form in the coldest ($T_K \sim 10\,K - 50\,K$) and densest ($n(H_2) \geq 10^4\,cm^{-3}$) molecular cloud environments and their resistance to freeze-out onto dust grains (Friesen 2019). CH_3OH (methanol) and SiO (silicon monoxide) are widely used as shock tracers in regions of star formation (Chahine et al. 2022). Methanol is primarily formed on the surfaces of dust grains through the hydrogenation of CO. Under normal conditions, it freezes onto grains and does not appear much in the gas phase. Shocks heat and sputter grain mantles, releasing CH_3OH into the gas phase (Rojas-García et al. 2022). Silicon is heavily depleted in molecular clouds, and it is locked in dust grain cores (silicates). Fast shocks ($\upsilon \geq 25\,km\,s^{-1}$) can destroy dust grains by sputtering or grain-grain collisions. Silicon is released into the gas phase and reacts rapidly with oxygen to form SiO (Rojas-García et al. 2022).

1.3 N_2H^+ as dense gas tracer

Molecular lines at mm-wavelengths provide information about the cold ISM ($\sim 10\,K - 50\,K$), because at these temperatures, most atoms/molecules are in low-energy rotational states where rotational transitions of molecules (e.g. CO(1-0), HCN(1-0), N_2H^+(1-0)) have energy level spacings corresponding to mm/sub-mm wavelengths. Arguably the most important dense molecular gas tracer is N_2H^+ (diazenylium). It is a key tracer because it forms in dense and cold regions with $n(H_2) \gtrsim 10^4\,cm^{-3}$ (Bergin & Tafalla 2007), where CO and other molecules start to freeze-out onto dust grains. Since N_2H^+ traces denser material than molecules like CO and NH_3 and is found almost exclusively in high-density regions with $n(H_2) \gtrsim 10^5\,cm^{-3}$ (Friesen 2019), it makes it a better tracer of star-forming cores.

N_2H^+ is ideal for molecular cloud observations for multiple reasons. Unlike the FIR/mm observation that trace the total column density, N_2H^+ observations trace only the column density of dense gas (Pety et al. 2017). It is important to note that N_2H^+ observations are not restricted to only stellar embryos, but also to more extended, larger dense environments such as filaments (Fernández-López et al. 2014). The ground-state emission transition $J = (1-0)$ is usually employed in dense core observations, since it is easily accessible with mm telescopes and the hyperfine splitting makes column density estimation more reliable (Caselli et al. 2002). The molecule remains in the gas phase even at very cold temperatures ($\sim$ 10 K), unlike many other molecules that freeze-out. As mentioned earlier, the N_2H^+(1-0) transition has seven total hyperfine components, where the first is a single hyperfine and the next three each make up two hyperfine triplets. Hyperfine structures, as well as narrow single lines, allow one to do high-precision measurements of gas kinematics (velocity, linewidths) and optical depth. Molecules such as ^{12}CO(1-0) suffer from becoming optically thick in dense gas, while N_2H^+(1-0) remains optically thin in many cases, providing a clearer view of velocity structures (Chen et al. 2025). Thus, it is less affected by opacity issues.

2 Orion Molecular Cloud 2

2.1 Orion A as study benchmark for molecular clouds

Star formation is one of the most important processes in the Milky Way. Stars are found to form along and at junctions of filaments within molecular clouds. The junction of multiple filaments is often referred to as a hub.

The most suitable region in space for studying star formation is the Orion A molecular cloud (see Fig. 2.1), located in the Orion molecular cloud complex. This is because Orion A is the closest and most active star-forming region in the local neighborhood of the Sun, located at a distance of 414 pc (Menten et al. 2007).

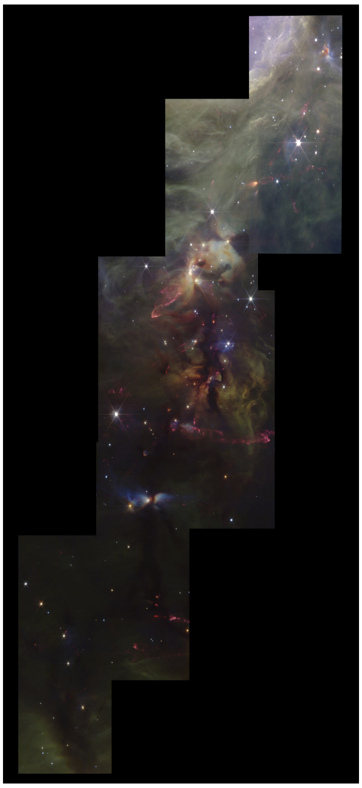

Figure 2.1: Northern Orion A cloud mosaic containing OMC-1, OMC-2, and OMC-3. The mosaic was taken by the JWST's NIRCAM instrument with f444w-f470n + f480m + f360m + f212n + f210m + f187n bands (Megeath et al. 2024).

The densest filamentary structure inside Orion A is the notorious $\sim 1.5^\circ$ long Integral Shaped Filament (Bally et al. 1987), also known as ISF (see Fig. 2.2). The ISF consists of < 1 pc small-scale sub-filaments (fibers) (Martin-Pintado et al. 1990; Shimajiri et al. 2011; Hacar et al. 2018) and hub-filament structures (hubs) (Mezger et al. 1990; Chini et al. 1997b; Hacar et al. 2018).

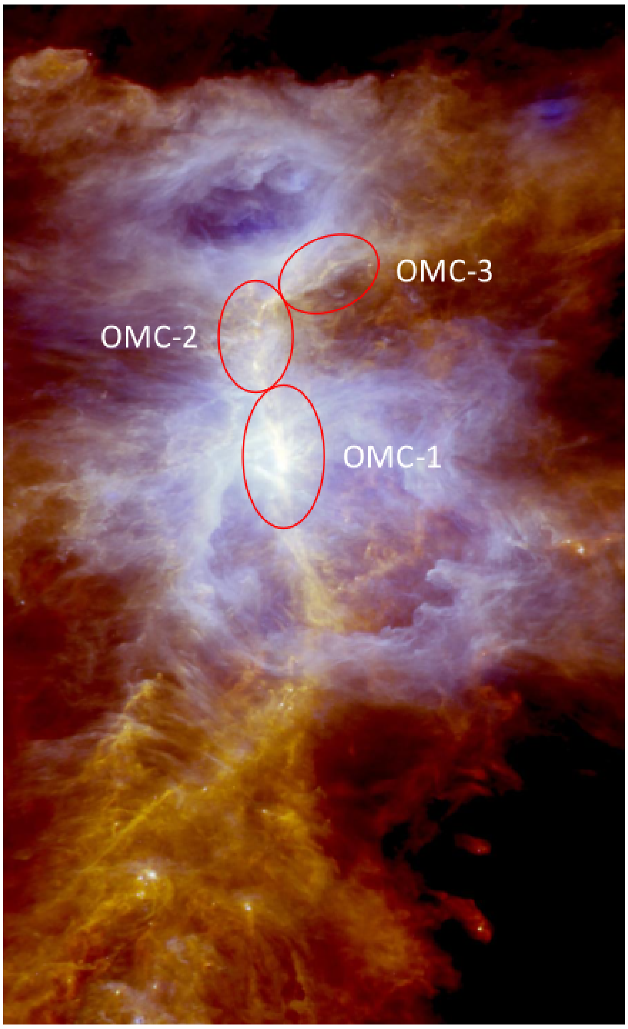

Figure 2.2: Infrared image of the ISF taken by Herschel. The image is a composite of the wavelengths of 70 μm (blue), 160 μm (green) and 250 μm (red) and spans about $1.3^\circ \times 2.4^\circ$. North is up and east is to the left. In red are circled the positions of OMC-1, OMC-2, and OMC-3. This image shows the glow of cosmic dust in the interstellar material that pervades the cloud, revealing an intricate pattern of filaments dotted with a few compact, bright cores: the seeds of future stars (Polychroni et al. 2013; André et al. 2014).

Inside of the ISF one can find the Orion Molecular Clouds (OMC-1 to OMC-4). OMC-1 lies behind the Orion Nebula M42 and the Trapezium stars and contains the massive star-forming region around the BN star and the KL nebula (O'Dell et al. 2008). North of OMC-1 one can find OMC-2 and further north OMC-3 (see Fig. 2.2).

The target region of this project is the Orion Molecular Cloud 2 (OMC-2), which is an active star-forming region within the ISF. Although OMC-1 is the brightest, most massive, and most studied part of the Orion Molecular Cloud, studying OMC-2 is equally important, since it gives insight to more Sun-like star formation processes. Thus, studying OMC-2 tests how a less massive environment changes star formation. Also, the less "turbulent" and dense environment allows us to study cores and filaments with less extinction.

The first definition of the OMC-2 region was when Gatley et al. (1974) discovered a group of near-infrared sources embedded in a molecular core, centered at a position of $\alpha = 05^{h}35^{m}26.8^{s}$, $\delta = -05^{\circ}10'17''$ (J2000). Thronson et al. (1978) estimated the total far-infrared luminosity of OMC-2 (IRS-3 and IRS-4) to be $2 \cdot 10^{3} L_{\odot}$, while Dutrey et al. (1993) found the molecular gas mass of OMC-2 to be $113\,M_{\odot}$. OMC-2/3 is located in the ISF extending northward from the Orion Nebula (NGC 1976) towards NGC 1977. An extended diffuse emission at 850 μm is detected in OMC-2, where molecular filaments are apparent in absorption (8 μm) against it (Peterson & Megeath 2008).

2.2 Intermediate mass protostars in OMC-2

OMC-2 is one of the nearest embedded cluster formation regions that has eleven infrared sources (Chini et al. 1997b) and includes intermediate-mass protostars ($2\,M_{\odot} < M < 8\,M_{\odot}$) at early stages of evolution. The study of the formation and evolution of such intermediate-mass protostars gives a crucial link between low-mass and high-mass star formation (Crimier et al. 2010). Intermediate-mass protostars share some properties of massive protostars, such as their ability to ionize the surrounding gas and that they exist in clusters. On the other hand, they have the advantage that they are more numerous and therefore are located at closer distances (< 1 kpc) than most of the massive star-forming regions (Gómez-Ruiz et al. 2019).

2.3 OMC-2 studies

OMC-2 has been studied thoroughly by astronomers in the past couple of decades. Six bright mm/IR sources (FIR 1-6) within a region of about 6′ in size have been identified by Mezger et al. (1990) (see Fig. 2.3). These sources have been associated with young stellar objects (YSOs) through the Herschel Orion Protostar Survey (HOPS) by Furlan et al. (2016). Observations of OMC-2 were made in the radio wavelength regime by Chini et al. (1997b) and Lis et al. (1998). For the near- and mid-IR regimes, observations were made by Tsujimoto et al. (2003), Nielbock et al. (2003), and Megeath et al. (2012).

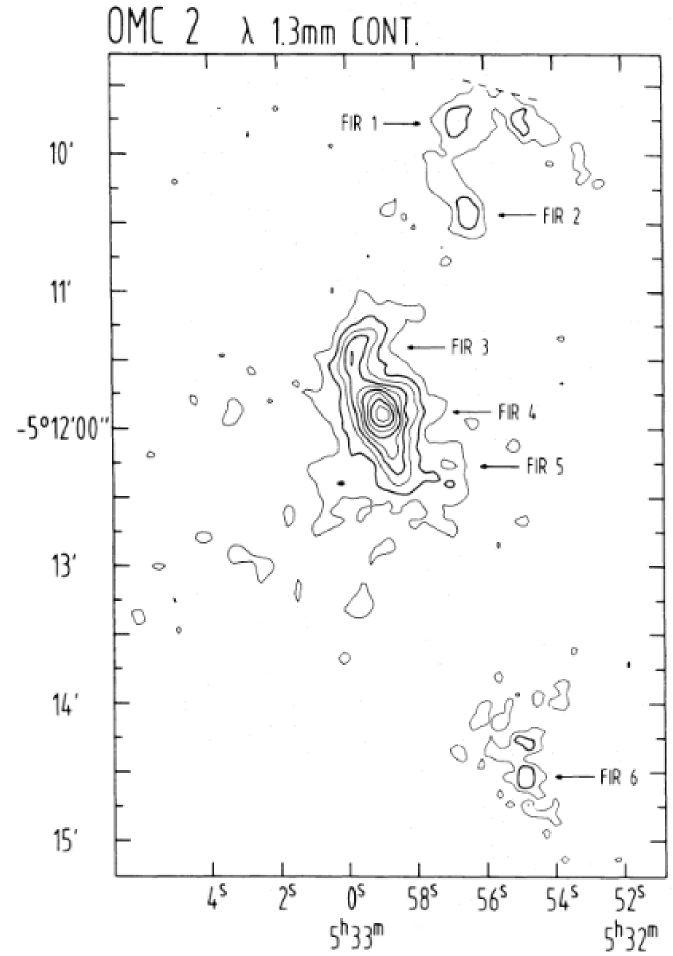

Figure 2.3: 1.3 mm continuum map of OMC-2 observed with the IRAM 30 m millimeter radio telescope (MRT). The position of the six FIR sources are shown (Mezger et al. 1990).

A total of 15 individual sources were identified through the 1.3 mm continuum observations within FIR 3, FIR 4 and FIR 5 with one Class 0, three Class I, three Class II, three flat spectra and five unclassified sources (Reipurth et al. 1999; Nielbock et al. 2003; Allen et al. 2007; Megeath et al. 2012; Stutz et al. 2013; Furlan et al. 2016; Osorio et al. 2017; van Terwisga et al. 2019). The brightest OMC-2 source in mm and sub-mm with a bolometric luminosity of $L_{\rm bol} \sim 1000\,{\rm L}_{\odot}$ (Crimier et al. 2009) is OMC-2 FIR 4, which has been associated with the HOPS-108 Class 0 protostar (Adams et al. 2012). Another potential protostar canidate for FIR 4 is HOPS-64 (Class I) (Furlan et al. 2016). A further bright source in the radio wavelength regime is OMC-2 FIR 3 (Chini et al. 1997a), also known as VLA 11 (Reipurth et al. 1999). FIR 3 was associated with the Class I intermediate-mass protostar HOPS-370, which has a well-collimated radio jet with a thermal free–free core (Osorio et al. 2017). HOPS-370 has been reported to have a dusty molecular disk structure around it (Tobin et al. 2020). The outflow driven by HOPS-370 is reported to have collided with the OMC-2 FIR 4 dust condensation, where the outflow interaction has impacted the star formation process in FIR 4 (Shimajiri et al. 2008). Furthermore, a cosmic-ray acceleration model explains the synchrotron emission along the jet in FIR 3 and the observed ionization rate of FIR 4 (Padovani et al. 2021). Clumping in OMC-2 has been reported by Batria et al. (1983), using temperature and radial velocity distribution maps of NH_3(1,1) & (2,2) inversion lines.

Investigating the internal structure and kinematics of filaments is of crucial importance for the description of the star formation process in the Milky Way. The internal substructure is important to study because stars form almost exclusively within dense substructures of these filaments, which are the hubs and cores. The study of the internal kinematics of filaments is a blueprint for mass assembly and gravitational collapse. Molecular observations have revealed that the intrinsic dense substructure of low-mass filaments in nearby clouds is a bundle of small-scale fibers (Hacar et al. 2013), which can have compact radial distributions narrower than the so-called universal 0.1 pc (Ishihara et al. 2024). This is of important relevance for OMC-2, as a complex fiber substructure within the OMC-2 FIR 4 hub has been identified by Chahine et al. (2022). The fiber network is also present in higher-mass regimes like the ISF (Hacar et al. 2018). Fibers are characterized by their continuity in space and velocity, transonic internal velocity dispersions along their typical length of $\sim$ 0.5 pc, and individual total masses per unit length consistent with hydrostatic equilibrium. The fibers harbor most of the cores within a certain region, which regulates the initial conditions for their gravitational collapse. The quiescent dynamical state of the fibers promotes the initial conditions for the subsequent gravitational fragmentation. The study of Hacar et al. (2018) suggests that the fibers in OMC-2 have an average length of 0.16 pc and typical widths of 0.2 pc – 0.5 pc. The dynamical state of the fibers is quiescent with a mean Mach number of 0.65, which means that the nonthermal velocity dispersion is quite smaller than the sound speed in that region.

3 ALMA

3.1 The ALMA Telescope

In this project, our main goal is to use ALMA's observations of N_2H^+ to study the dense gas structure and kinematics in OMC-2. Our secondary goal is to use other ALMA observations of different molecular tracers to have a full gas (& dust) structural and kinematical description of the OMC-2 region. In the following sections, we will explain what ALMA is and why it is such a powerful array.

The Atacama Large Millimeter/Submillimeter Array (ALMA) is an aperture synthesis telescope (interferometer) that operates over a broad range of observing frequencies in the millimeter and submillimeter regime of the electromagnetic spectrum. ALMA is located in the Chajnantor plain of the Chilean Andes (latitude = −23.02917°, longitude = −67.754649°), which is a place that usually offers exceptional dry and clear sky conditions that are required to observe in the mm/sub-mm regime (see Fig. 3.1).

Figure 3.1: ALMA antennas on the Chajnantor Plateau (Cortes et al. 2023).

The array is composed of 66 high-precision antennas that are subdivided into three sub-arrays:

- The 12-m Array consisting of fifty 12-m antennas
- The 7-m Array consisting on twelve 7-m antennas
- The Total Power Array (TP Array) consisting of four 12-m antennas

The union of the 7-m Array and the TP Array is often referred to as the Atacama Compact Array (ACA).

The 12-m Array is used for sensitive and high-resolution imaging, recovering the emission at the smallest scales. To achieve a certain angular resolution, the antennas can be positioned in up to ten different configurations. This is made possible by 192 antenna foundations (stations) that are distributed over the Chajnantor and Pampa la Bola plateaus. The distribution of stations produces distances between two antennas (baselines) ranging from 15 m to ~ 16 km. The angular resolution achieved by ALMA is roughly limited by the longest baseline ($L_{\max}$) through $\sim 0.2'' \times (300/\nu[\mathrm{GHz}] \times (1\mathrm{km}/L_{\max})$, where ν is the frequency given in GHz. ALMA can observe most frequency ranges from 35 GHz to 950 GHz through 10 receiver bands. Band 2 (67 GHz to 84 GHz) is not yet available.

However, the TP Array recovers the emission at the most extended spatial scales, resolving the short-spacing problem (see Sect. 4.5). The TP Array provides full spatial information samples from 0 m to 12 m as autocorrelations. This is not surprising because TP antennas are single-dish antennas with a diameter of 12 m. The spatial sampling gap between the 12-m Array and the TP Array is covered by the 7-m Array, which samples baselines from 9 m up to 30 m (Cortes et al. 2023).

3.2 ALMA as the ideal telescope to study molecular clouds

ALMA is the best telescope for studying molecular clouds such as OMC-2 because of its unmatched sensitivity, resolution, and frequency coverage in the mm/sub-mm regime. This is relevant for this project, since the dense gas tracer N_2H^+(1-0) is exactly in that regime ($\nu = 93.173\,764$ GHz).

The first big advantage over other radio telescopes is its exceptional angular resolution, where the array achieves angular resolutions down to $\sim 0.005''$ in the most extended configurations. For example, with an angular resolution of $1''$ one can study small-scale structures in OMC-2, such as dense cores, filaments, disks, and outflows, at a spatial resolution of ~ 0.002 pc, because the typical sizes of these objects are significantly larger. The second advantage is its high sensitivity to molecular emission. ALMA's high sensitivity allows it to detect faint molecular lines in a short amount of time, adequate for the allowed observation time an astronomer gets. This is crucial for studies of low abundance species and weak isotopologues, which help probe the chemistry and physical conditions in molecular clouds. Another advantage is that ALMA has a wide frequency coverage (35 GHz - 950 GHz). ALMA can observe in multiple bands, covering the mm and sub-mm wavelengths where molecular rotational transitions occur. This is because the cold gas in a molecular cloud excites only rotational transitions and not vibrational or electronic transitions. The energy values for electronic, vibrational and rotational transitions correspond to ~ 10 eV, 0.1 eV, and 0.001 eV, or wavelengths of ~ 100 nm (optical/UV), 10 µm (near/mid-infrared) and 1 mm (radio) (Williams 2021). Usually low rotational transitions such as the $J = 1 - 0$ (e.g. N_2H^+, CO, HCN) or the $J = 2 - 1$ (e.g. CO, SiO) are found in the radio regime. Furthermore, ALMA provides high spectral resolution (up to $\Delta v \sim 0.01\,\mathrm{km\,s^{-1}}$), allowing detailed velocity studies of gas motions. This is crucial for mapping gas inflows, outflows, turbulence, and fragmentation within a molecular cloud, helping to understand star formation processes. The last big advantage over most radio telescopes is ALMA's ability to combine interferometric and TP (single-dish) observations, which allows it to study both small-scale dense cores and large-scale cloud structures, for which it was specially designed (Cortes et al. 2023).

3.3 ALMA observations of OMC-2

Since ALMA became operational, the OMC-2 region has been extensively observed. ALMA observations of protoplanetary disks at 856 μm have revealed a total of three protoplanetary disks in OMC-2, two of them near OMC-2 FIR 4 and one of them in OMC-2 south (Mann et al. 2014). Kainulainen et al. (2017) detected 36 dense cores in OMC-2 using ALMA 3 mm continuum emission observations, where ∼ 60% of the cores are protostellar and ∼ 40% are starless cores. Hacar et al. (2018) combined N_2H^+(1-0) ALMA and IRAM observations of the ISF to infer a braided fiber network, which explains the complex substructure of dense gas in the ISF, as well as its current distribution of cores and protostars. A total of 27 coherent velocity fibers were found in OMC-2 (see Fig. 3.2). Sato et al. (2023) used CO(2-1) line emission from ALMA to identify 12 outflows in the FIR 4 region, SiO(5-4) line emission to trace shocked gas structures and 1.3 mm dust continuum observation to identify 51 dense sources in the OMC-2 region. ALMA 1.3 mm dust continuum data were utilized to construct dust SED in the mm to cm range of seven solar-like protostars in OMC-2 (Bouvier et al. 2021). A twin jet structure from HOPS-60 (OMC-2 FIR 6b) has been characterized by the analysis of Soker et al. (2022), where ALMA CO(2-1) and 1.3 mm continuum data have been employed. A highly collimated SiO jet (∼ 1°) with a projected length of ∼ 5200 au from the embedded protostar VLA 15 was revealed (Chahine et al. 2022). Fontani et al. (2020) observed nitrogen bearing molecules with ALMA in OMC-2 FIR 4 to derive the isotopic $^{14}N/^{15}N$ ratio and concluded that the ratio does not change across the region at core scales and does not depend on temperature variations.

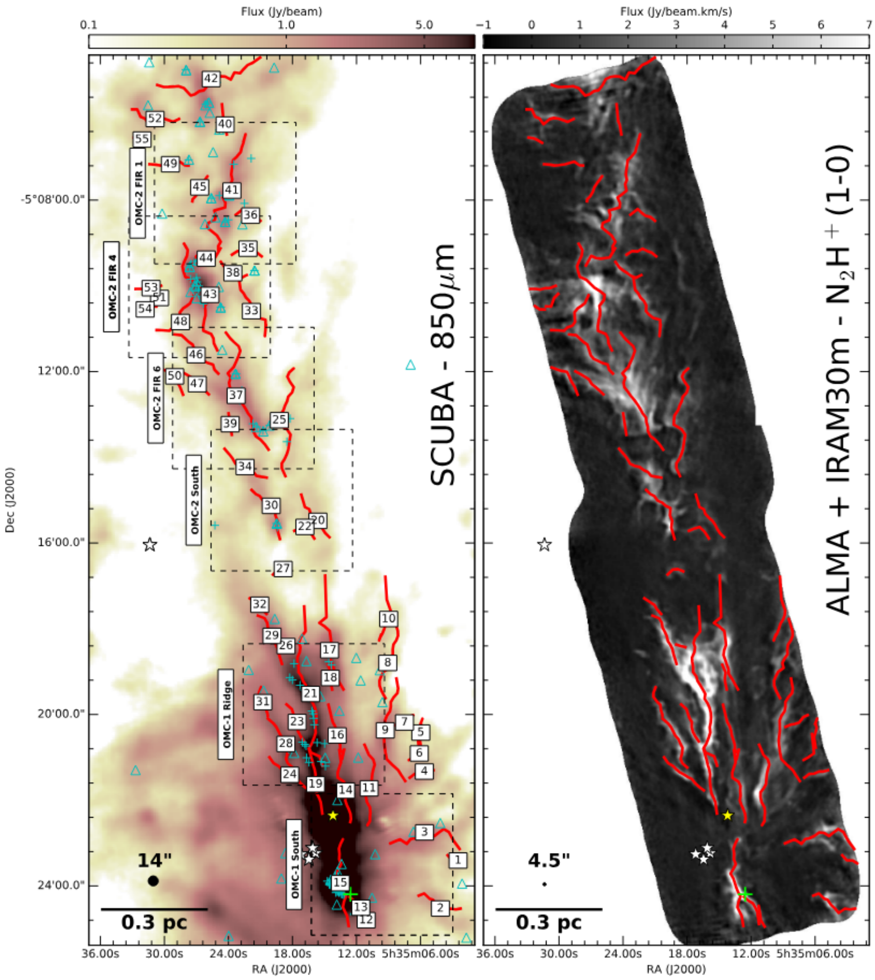

Figure 3.2: Main axis of the 55 fibers identified by the HiFIVE analysis along the ISF (red segments). (**Left**) SCUBA-850 µm continuum emission (Johnstone & Bally 1999). (**Right**) Total N_2H^+ integrated emission. The position of both protostars (blue triangles) and continuum sources (blue crosses). For reference, the positions of the Trapezium and NU Ori stars (white stars) plus the Orion BN source (yellow stars), are highlighted in both panels. The corresponding beamsizes are indicated in the lower left corner in comparison with a characteristic 0.3 pc scale (black bar). The position of the regions in OMC-2 and OMC-1 are shown as enclosed dashed boxes in the SCUBA map (Hacar et al. 2018).

4 Interferometry

4.1 Introduction to interferometry

Radio telescopes like ALMA can obtain very high angular resolution observations of astronomical phenomena through a technique called interferometry. Interferometry is, in essence, the combination of sky signals received by two or multiple physically separated antennas. A sky brightness distribution is sampled on an angular scale smaller than possible with a single antenna when the signals from different antennas interfere with each other. The angular sensitivity of the antennas is modified through this interference, which gives rise to a sinusoid of constructive and destructive nodes. A visibility, which is a datum of the interferometer, consists of the following two measures:

- Measure of the brightness of the emission on the angular scale sampled (related to the amplitude of the sinusoid)
- Measure of the relative position of that brightness on the sky (related to the phase of the sinusoid)

By including many pairs of antennas with different relative orientations in an array, a large number of discrete angular scales can be sampled. The rotation of the Earth can be used to change the projected separations of the antenna pairs, which leads to more angular scales to be sampled when tracking a source across the sky. This sampling, which arises from the visibility measurement made by an interferometer, occurs in the so-called Fourier space. Once the sinusoids of various amplitudes and phases are sampled, one can use the Fourier transform to sum the data set to produce an image of the sky brightness distribution in the so-called Image space. In essence, the Fourier transform is used to reconstruct the desired sky brightness distribution from the "raw" visibility data taken by the interferometer. The more angular scales and directions that have been sampled, the better the image reflects the actual sky brightness distribution (Cortes et al. 2023).

4.2 Antenna Response

To understand what and how radio antennas capture signals, the concept of received power P_{rec} must be introduced. The power received P_{rec} from a radio telescope from an unpolarized source is given by:

$$P_{\text{rec}} = \frac{1}{2} I_\nu A_e \delta\Omega, \tag{4.1}$$

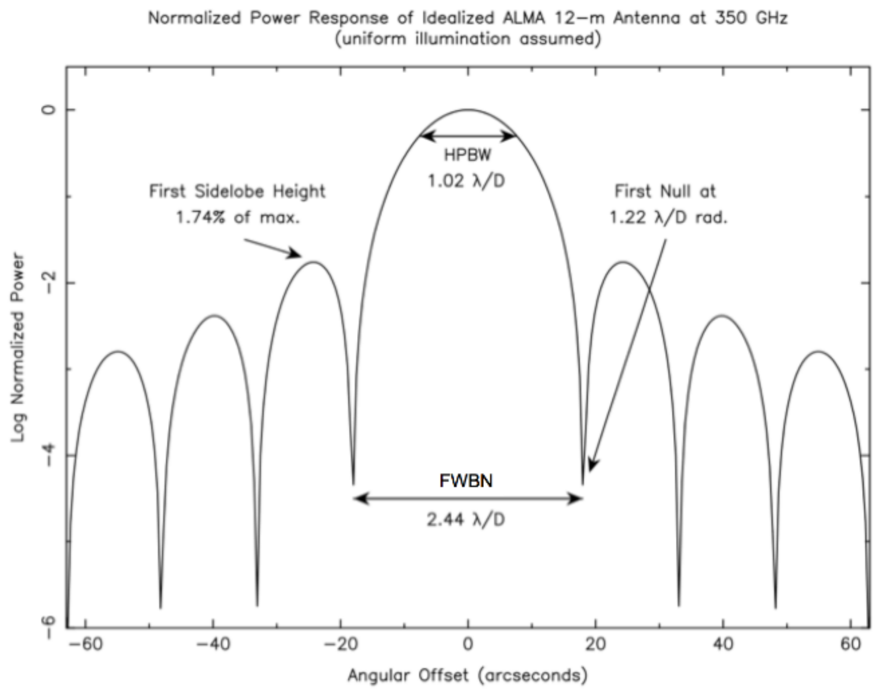

Figure 4.1: Normalized 1-D antenna power response for a 12-m antenna uniformly illuminated at 350 GHz from Cortes et al. (2023).

where I_ν is the specific intensity, A_e is the effective area of the radio telescope and $\delta\Omega$ is the solid angle. Usually, the receiver is sensitive to only one mode of polarization, thus the factor of 1/2. In the case of ALMA there are two independent receptors so that both modes of polarization can be detected simultaneously (the coefficient is 1).

The integration of the specific intensity over the solid angle of the emitting source is defined as the flux density S_ν:

$$S_\nu = \int I_\nu \, \mathrm{d}\Omega. \tag{4.2}$$

I_ν has units of W m^{-2} Hz^{-1} sr^{-1}, while S_ν has units of W m^{-2} Hz^{-1}. Since the received power for radio sources is usually very weak, a new unit for the flux density is introduced to illustrate this, namely the Jansky (Jy), where 1 Jy=10^{-26} W m^{-2} Hz^{-1}.

After reflection off the primary surface, the electromagnetic (EM) power is brought to a focus by the corresponding antennas. The sum of all the EM power is the so-called antenna response (relative sensitivity), which is dependent on the incoming phase front angle. When the incoming phase front angle is not perpendicular to the on-axis pointing direction of the antenna, one gets diffraction (self-interference).

Fig. 4.1 shows an example of the antenna power response in one dimension. For on-axis incoming waves, the EM power adds coherently, maximizing the response. This is seen centrally as the main lobe (known as the primary beam), which is approximately Gaussian. For off-axis waves, the effective antenna diameter decreases, reducing sensitivity. These can be seen as the multiple weak sidelobes which also have this Gaussian-like feature. An associated quantity to the primary beam is the Half Power Beam Width (HPBW) given by:

$$\text{HPBW Primary Beam} = 1.02 \times \frac{\lambda}{D}, \tag{4.3}$$

where λ is the wavelength and D the diameter of the antenna. With increasing angular scales, the antenna response repeatedly increases and decreases (constructive and destructive interference), which corresponds to the sidelobes. The minima between the primary beam and sidelobes are called nulls. Even if the sidelobes have only 1% of the response of the primary beam, a bright incident emission at angles corresponding to those sidelobes gives enough EM power to contaminate a potential reconstructed image with artifacts.

All of the above is the description of an idealized antenna, while the actual antenna response is affected by various effects. These are surface imperfections, degree of secondary illumination, and diffraction by the arms supporting the secondary (Cortes et al. 2023).

4.3 Aperture Synthesis Technique

In the millimeter/submillimeter regime (radio) observations have lower resolutions than optical wavelength SD observations because of the larger wavelength. On the other hand, the diameter of radio SD telescopes can be larger than that of optical SD telescopes, but one cannot obtain angular resolutions better than $1''$.

Interferometry combines signals from multiple physically separated antennas to achieve higher angular resolution for radio frequencies, basically emulating the effect of having a single radio telescope with a very large diameter. This technique is also commonly referred to as aperture synthesis and was pioneered by Sir Martin Ryle (Nobel Prize in Physics in 1974). The major problem with aperture synthesis is that only certain angular scales will be sampled. These angular scales are determined by the projected separations of each pair of antennas.

When a plane-parallel wavefront arrives at the antennas on-axis, the EM power in phase is focused correctly. The power is proportional to the measured voltages $V(t)$ of the antennas through the following expression (see the derivation in Cortes et al. (2023)):

$$\langle P \rangle \propto \sum \langle \Delta V_i^2 \rangle + \sum \sum_{i \neq k} \langle \Delta V_i \Delta V_k \rangle. \tag{4.4}$$

The first term of this equation are the autocorrelation elements, while the second term are the cross-correlation elements. The autocorrelation term refers to the correlation of the received signal with itself at the same antenna or signal channel. Mathematically, it is a measure of how signal power varies over time in a single antenna or element. Cross-correlation refers to the correlation of the received signals between two separate antennas or elements. It measures how similar the signals are across different antennas or baselines (distance between two antennas), and is a fundamental aspect of interferometry.

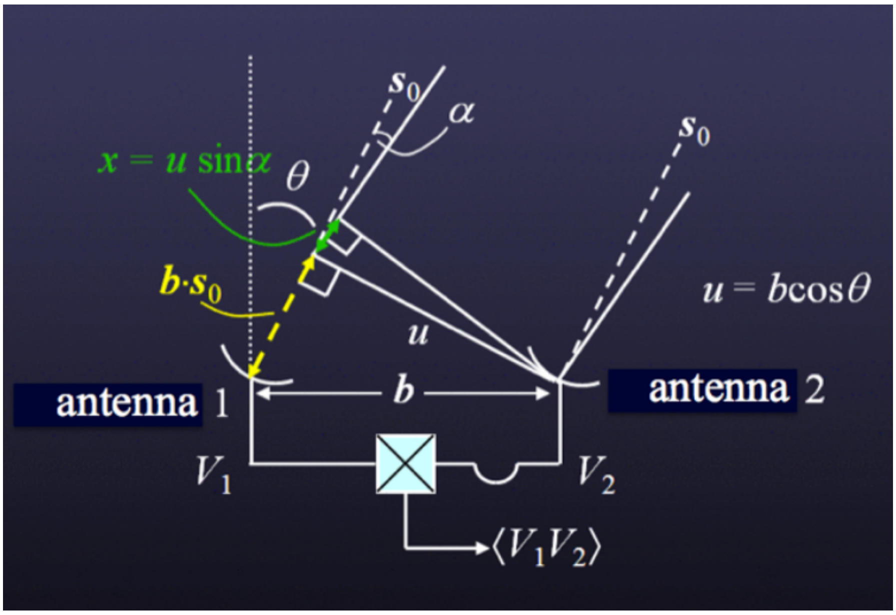

Figure 4.2: Schematic view of an ideal 1-D interferometer consisting of two antennas from Cortes et al. (2023).

Since emission can reach the antennas from other directions, the induced phase differences have to be taken into account (see Fig. 4.2). Assuming that the wavefront arrives first at antenna 2, one can relate both voltage responses in 2-D through an exponential delay factor (see the derivation in Cortes et al. (2023)):

$$V_2 = V_1 \, e^{2\pi i(ul+vm)}. \tag{4.5}$$

Once the voltages of both antennas are determined, these are combined in the correlator, which is connected to the two antennas. The output of the correlator, which multiplies and time-averages the incoming signals, is given as follows:

$$\langle V_1 V_2 \rangle = \langle \iint V_1(l,m) \, \mathrm{dl\,dm} \iint V_2(l,m) \, \mathrm{dl\,dm} \rangle. \tag{4.6}$$

Knowing that $V^2 \propto P$ (see Eq. 4.4) and $P \propto I_\nu$ (see Eq. 4.1) one finally gets the description of the complex visibility $\mathcal{V}$ that is measured from the correlator and is nothing else than the Fourier transform of the intensity distribution on the sky (see the derivation in Cortes et al. (2023)):

$$\mathcal{V}(u,v) = \iint I(l,m) e^{2\pi i(ul+vm)} \, \mathrm{dl\,dm} \rangle = A \exp^{i\phi}. \tag{4.7}$$

The equation above proves that the complex visibility is just dependent on an amplitude A and a phase ϕ. At certain spatial frequencies u and v, A contains information about the source brightness and ϕ about its location relative to the phase center (Cortes et al. 2023).

4.4 The Visibility or (u, v) Plane

The basis of the aperture synthesis technique is the van Cittert-Zernike theorem, which relates the sky brightness distribution with the complex visibility distribution. In the image plane, the complex visibility is described by the Fourier transform of the sky brightness distribution. On the other hand, in the visibility plane the sky brightness distribution is described by the inverse Fourier transform of the complex visibility distribution:

$$\begin{aligned} \mathcal{V}(u, v) &= \iint I(l, m) e^{2\pi i(ul+vm)} \, \mathrm{dl}\, \mathrm{dm} \\ I(l, m) &= \iint \mathcal{V}(u, v) e^{-2\pi i(ul+vm)} \, \mathrm{du}\, \mathrm{dv}. \end{aligned} \tag{4.8}$$

By measuring the visibilities in the (u, v) plane, it is possible to reconstruct the brightness distribution of the sky, as they are Fourier conjugates. Each visibility point in the (u, v) plane represents a specific spatial frequency, which corresponds to an angular scale of emission in the sky. An interferometric image is the result of combining all visibility measurements, where each visibility represents the brightness and position of emission at a particular angular scale. To fully reconstruct the sky brightness distribution, a well-sampled (u, v) plane is required, which improves image accuracy and resolution. A single pair of antennas samples one spatial frequency in the (u, v) plane per observation, but generates two visibilities due to Hermitian symmetry. The first is located at (u, v) and the second is located at the conjugate complex of the first, which is $(-u, -v)$.

Adding antennas in an array and distributing them in both the u and v directions increases the number of independent baselines (physical distances between antennas), improving the (u, v) coverage. An array with N antennas has $N(N-1)/2$ unique baselines, each providing a unique sample in the (u, v) plane. Furthermore, Earth's rotation can be used to sample more from the Fourier plane. As the Earth rotates, the projection of each baseline changes, allowing repeated observations of a target to sample different points in the (u, v) plane. Using multiple antenna configurations can also increase the (u, v) plane coverage. By arranging antennas at varying distances, different parts of the (u, v) plane can be sampled (Cortes et al. 2023).

4.5 Field-of-view and Spatial Filtering

Every antenna in an interferometer has a finite diameter, which limits the field-of-view of an observation because of the antenna's power response. For an unobstructed, uniformly illuminated aperture, the power response is equal to the Airy function $P_N = \mathcal{A}(l, m)$. The Half Power Beam Width (HPBW) of this primary beam defines the effective field-of-view for a single interferometric pointing.

The antenna power response $\mathcal{A}(l, m)$ influences the visibility measurements in an interferometer, as it is included in the visibility integral:

$$\mathcal{V}(u, v) = \iint \mathcal{A}(l, m) I(l, m) e^{-2\pi i(ul+vm)} \, \mathrm{dl}\, \mathrm{dm}. \tag{4.9}$$

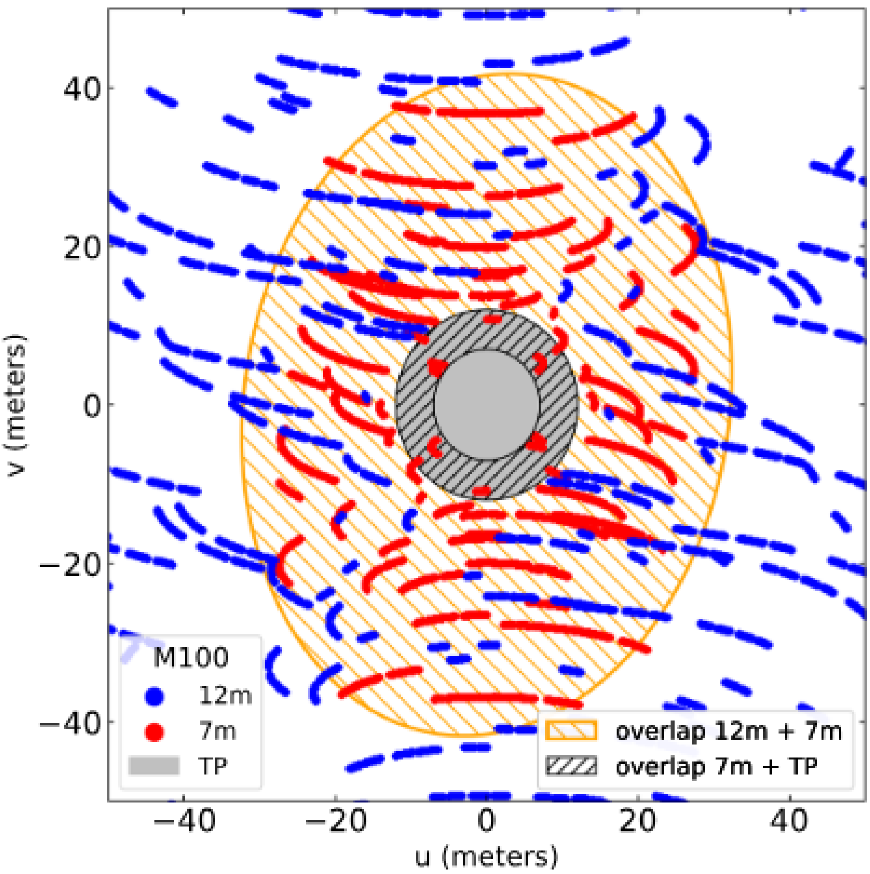

Figure 4.3: Central (u, v) coverage of the M100 data set presented in Plunkett et al. (2023) showing all baselines of ≤ 50 m observed by the 12-m (blue), 7-m (red), and TP (gray) arrays.

Since an interferometer captures the Fourier transform of the sky brightness $I(l, m)$ weighted by the primary beam response $\mathcal{A}(l, m)$, recovering the true sky brightness requires dividing the processed image by the primary beam response. This step is known as primary beam correction and ensures accurate flux densities, especially for sources far from the phase center.

In practice, it is impossible to fully sample the (u, v) plane, which limits the achievable resolution and introduces spatial filtering effects. An incomplete (u, v) sampling restricts the level of detail in an image and affects the accuracy of the sky brightness distribution. Insufficient short baselines result in reduced sensitivity to large-scale emission, because the extended emission is filtered out. The reconstructed image looks artificially fragmented, almost as if the interferometer would not "see" the smooth extended background and largest scale structures. This problem is known as the "short spacing" problem, which can be seen as a "hole" in the inner region of the (u, v) coverage (see Fig. 4.3).

The impact of the short-spacing problem is not just restricted to the continuum images, but also spectral images can also be strongly affected (Rau & Cornwell 2011). Complementing the interferometric observations with a separate SD telescope observation (sensitive to large scales) using data combination is the go-to solution. As a rule of thumb, the SD telescope's diameter should be greater than or at least equal to the interferometer's shortest baseline. This is because now the hole in the (u, v) plane is fully covered, recovering the most extended structures. In the case of ALMA one can do this by combining data from the main ALMA 12-m array and/or the ALMA 7-m Compact Array (ACA) with data from the ALMA total power (TP) telescopes (Plunkett et al. 2023). An even quantitatively better result for the reconstructed image can be obtained by combining a larger SD telescope, like the IRAM 30-m telescope (see discussion in Bonanomi et al. (2024) and work of Hacar et al. (2018)).

When sampling a discrete amount of visibilities, the (u, v) plane distribution is represented as a set of delta functions. The image derived from these discrete samples, called the dirty image, is effectively a convolution of the true sky brightness distribution with the point spread function (PSF), which is the inverse Fourier transform of the sampling function (u, v). The PSF is often known as the synthesized beam or the dirty beam. The dirty image $I^D(l, m)$ is mathematically expressed as:

$$I^D(l, m) = b(l, m) * I(l, m)\mathcal{A}(l, m), \tag{4.10}$$

where $b(l, m)$ is the dirty beam, representing the Fourier transform of the sampled (u, v) plane distribution, $I(l, m)$ is the intensity distribution of the sky, and $\mathcal{A}(l, m)$ is the antenna's primary beam response. Artifacts, such as sidelobes, appear because of incomplete sampling, causing bright spots to be distributed by the dirty beam across the image. Deconvolution algorithms such as CLEAN (Högbom 1974) reduce these effects and help improve image quality by accounting for missing (u, v) data. Image fidelity is a measure of the similarity of an image with its true sky distribution. A better (u, v) coverage leads to higher image fidelity and with fewer artifacts in the reconstructed image.

The resolution is often approximated by the Full Width Half Maximum (FWHM) of a Gaussian fit to the central lobe of the dirty beam. Compact configurations produce larger beams and lower resolution due to clustering near the (u, v) origin, whereas widely spaced baselines produce higher resolution with narrower beams. The smallest detectable detail in the sky brightness distribution is the minimum resolvable scale, which is determined by the longest baseline:

$$\text{Interferometer Resolution} = \theta_{\text{res}} = k\frac{\lambda}{L_{\text{max}}}, \tag{4.11}$$

where k is a weighting factor (typically ~ 1) and L_{max} is the longest baseline in the array. To effectively improve the spatial resolution of an interferometer, the most obvious thing is to increase the maximum baseline L_{max}, because the resolution of the interferometer depends on it. This is simply done by extending the physical separation of the antennas. Another way is to use higher observing frequencies. Since $\lambda = c/\nu$, observing at shorter wavelengths (higher frequencies) improves resolution. Furthermore, observing the same source over longer time periods (earth rotation synthesis) helps fill gaps in the (u, v) plane. Using multi-configuration observations (combining data from compact and extended configurations) improves beam quality. Lastly, since the resolution depends on the weighting and synthesis effects given by k one might use super-resolution techniques. Algorithms like MEM (Maximum Entropy Method) or nonparametric deconvolution can enhance resolution beyond the nominal interferometric limit.

The largest angular scale an interferometer can recover, known as the Maximum Recoverable Scale (MRS), is constrained by the shortest baseline:

$$\text{Maximum Recoverable Scale} = \theta_{\text{MRS}} \approx 0.6\frac{\lambda}{L_{\text{min}}}, \tag{4.12}$$

where L_{min} is the minimum baseline in the array. ALMA uses the 5th percentile shortest baseline L_5 instead of the very shortest baseline L_{min} to calculate the MRS ($\theta_{\text{MRS}} \approx 0.983\frac{\lambda}{L_5}$). Large-scale emission is underrepresented or absent in images when spatial frequencies near the (u, v) origin are unsampled. This makes interferometers best suited for compact or small-scale sources. Overcoming the maximum recoverable scale limit is essentially recovering more and more large-scale emission. As explained in a previous section, one way to recover large-scale emission is to combine interferometric observations with single-dish observations, overcoming the short-spacing problem. A thought solution to minimize the lack of sensitivity at large scales is to put several antennas really close together. The problem of tightly packing antennas (especially at low elevations) is that one antenna may partially block another, reducing the data quality of that pairing due to interference. This phenomenon is known as shadowing. Shadowed data are usually removed during image processing to maintain accuracy in the final image. Moreover, mosaic observations are really helpful to overcome the limited sensitivity. This occurs when observing with overlapping pointings in a hexagonal grid that will increase the effective field of view while retaining high resolution (Cortes et al. 2023).

All of these concepts and interferometric properties will be useful for the project. Once we have the ALMA visibility data for OMC-2, we will use an algorithm (see Sect. 5.3) to transform the sampled Fourier space into the desired sky brightness distribution image. We will use data combination techniques (see Sect. 5.4) on the resulting image and a SD-image of OMC-2 to preserve sensitivity at a high angular resolution. The final image should represent the "true" sky brightness distribution of OMC-2 as closely as possible.

5 Analysis

5.1 Data mining

In this project, we will make use of the ALminer toolkit (Ahmadi & Hacar 2023) for efficient mining of the ALMA Science Archive to explore the molecular content of the OMC-2 region. ALminer[1] is a novel Python-based code that enables users to efficiently query, analyze, and visualize the metadata of the ALMA Science Archive. Our first goal of the project is to find all relevant N_2H^+(1-0) projects in OMC-2, as N_2H^+ is the target tracer. ALminer offers three possible ways to query metadata:

- Query by target name
- Query by position
- Query by ALMA keywords

Of the three methods, we chose the second one, since querying by position can be simply done by knowing the RA and Dec coordinates of OMC-2. From the literature (Gatley et al. 1974) it is known that OMC-2 has central coordinates at $\alpha = 05^{\mathrm{h}}35^{\mathrm{m}}26.8^{\mathrm{s}}$, $\delta = -05^\circ 10' 17''$ (J2000). We inserted the aforementioned RA and Dec values in the ALminer *conesearch* function with a search radius of $6'$, which ensured complete coverage of the OMC-2 region. The query results were given in the form of a PANDAS DataFrame and could be explored in the form of a table. This table contains 88 columns of metadata information for the projects found in the query. The most important columns contain information about the project code, source name, coordinates, angular and spectral resolution, central frequency, and bandwidth. Since N_2H^+(1-0) is the tracer of interest, we further narrowed down the search results to only that tracers frequency, with N_2H^+(1-0) having a central frequency of 93.173 764 GHz. We used the PANDAS Dataframe functions to achieve that. We found a total of four projects, where only three of them contained two subbands each of the OMC-2 observations. We analyzed all of the remaining subbands in the fundamental metadata parameters to assess whether these observations should be taken into consideration for the latter kinematic analysis. The criteria we checked are that the angular resolution must be at least $5''$ and the spectral resolution of at least $0.5\,\mathrm{km\,s^{-1}}$. One subband of each of the three projects passed the criteria check. ALminer allows the download of archive data products, such as the continuum maps from the queried result projects. We checked last on these continuum maps of the three projects. The maps of two projects showed the expected OMC-2 region in both high and low resolution, while the remaining continuum map showed poor 7-m ALMA data for the OMC-3 region. This meant that there was a mislabeling of the source name

[1] https://nbviewer.org/github/emerge-erc/ALminer/blob/main/notebooks/tutorial/ALminer_tutorial.ipynb

of that specific project, which led that project to be discarded. In conclusion, we chose two final N_2H^+(1-0) projects with one subband each for further analysis (see Tab. 5.1).

Project code	Source name	Ang. Res. (″)	Vel. Res. ($km\,s^{-1}$)	Bandwidth (GHz)
2015.1.00669.S	OMC_2	2.565	0.098	0.059
2016.1.00681.S	OMC2-FIR4	1.645	0.195	0.059

Table 5.1: Table of final N_2H^+(1-0) projects in OMC-2 with project code, source name, angular resolution in ″, velocity resolution in $km\,s^{-1}$ and bandwidth in GHz.

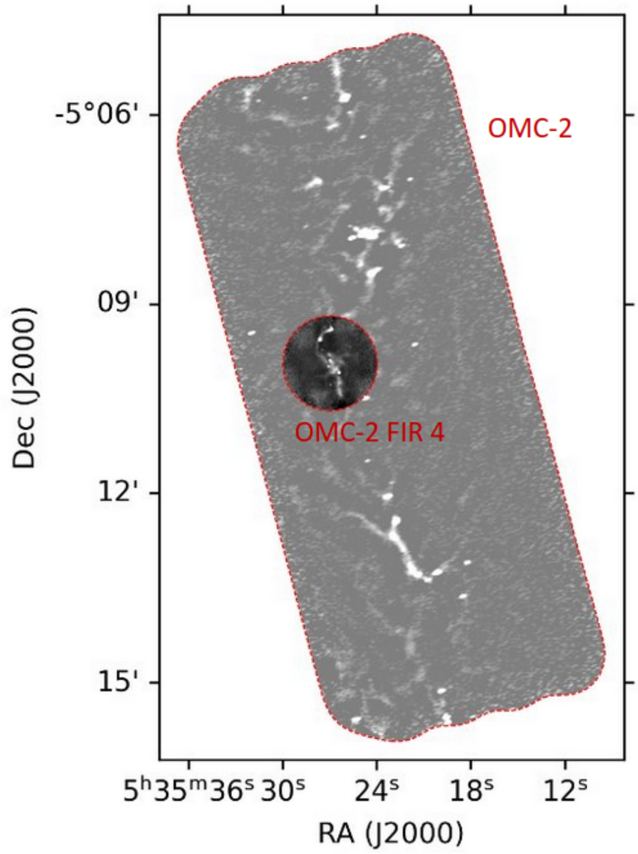

Figure 5.1: Spatial coverages of the 2015.1.00669.S project continuum map and the 2016.1.00681.S project continuum map, showing the sizes of OMC-2 and OMC-2 FIR 4, respectively.

As one can see from the source names, the 2015.1.00669.S project comprises the entire extent of OMC-2, while the 2016.1.00681.S project encompasses only the tiny region around the FIR 4 source in OMC-2 (see Fig. 5.1). The reason why we kept the FIR 4 project is because it has a better angular resolution than the OMC-2 project, even though the spectral/velocity resolution is worse. Based on these observations, the goal of our project is to combine these two projects with modern data combination techniques for the FIR 4 region (overlapping region). By doing this, we can keep the solid angular resolution of the FIR 4 project, but also gain a lot of sensitivity at the more extended scales with the OMC-2 project. The "only" price to pay is that we have to take the worse spectral resolution of the two.

The next step was to retrieve the visibilities of the two projects. The 2015.1.00669.S project has an already publicly available total integrated intensity N_2H^+(1-0) combined mosaic of the Integral Shape Filament (ISF). We downloaded the appropriate FITS datacube from the ORION-4D website[2] (Hacar et al. 2018). However, we requested the visibilities of the 2016.1.00681.S project through the ALMA Science Archive help center. We obtained the calibrated MS files by providing the MOUS uid's through a helpdesk. The total number of visibilities amounts to seven, where three of them come from the 12-m Array and the other four from the 7-m Array.

5.2 Other molecular projects

One of our goals in the project is to collect the largest possible database of ALMA observations in this region. We achieved this goal by using ALminer to extract all possible molecular metadata from OMC-2. In the previous section, our goal was to mine all possible N_2H^+(1-0) data, where we narrowed the search for that specific tracer using its frequency. To find the whole set of molecular OMC-2 observations, we look at the initial query result table. We discarded projects that are not part of the OMC-2 observations. We then used ALminer's *plot_overview* function to look at the number of observations per frequency (ALMA band 3 to 7). Molecules such as CO and its isotopologues are marked in the observations plot. This made it easier to associate the molecule with certain projects. For all other observations, we used the splatalogue[3] as an aid to find the molecule associated with the projects. The molecular projects found in this work are listed in Tab. 5.2 (one project per molecule).

Molecule	Project code
CO(2-1)	2017.1.01353.S
^{13}CO(2-1)	2023.1.01643.S
C^{18}O(2-1)	2016.1.00376.S
HCN(1-0)	2022.1.00513.S
CS(2-1)	2013.1.01114.S
N_2D^+(2-1)	2016.1.00681.S
$CH_3OH(5_{1,4} - 4_{1,3})$	2016.1.00376.S
SiO(6-5)	2016.1.00376.S

Table 5.2: Table of other molecular projects in OMC-2 with molecule and project code.

[2]https://sites.google.com/site/orion4dproject/data
[3]https://splatalogue.online//#/advanced

Molecules, other than N_2H^+(1-0), that were important for our physical interpretation of the cloud are CO(2-1) (see Sect. 6.6), $CH_3OH(5_{1,4} - 4_{1,3})$ (see Sect. 6.5) and SiO(6-5) (see Sect. 6.5).

5.3 Spectral line imaging

Spectral line imaging on the calibrated visibilities is an essential part before performing any type of data combination. We performed the whole procedure with the Common Astronomy Software Applications (CASA) package (CASA Team et al. 2022) and used the 6.5 version of CASA for this work.

5.3.1 UV continuum subtraction

The very first step in spectral line imaging is the UV continuum subtraction, i.e., the removal of continuum emission from the visibilities (u, v) data. The continuum spans over most spectral channels, but in some there is spectral line emission. Ideally, the UV continuum subtraction is done by fitting the amplitudes using only those spectral channels that are free from spectral line emission. Some channels in the continuum might have a mild frequency dependence, but those will not distort the outcome[4].

We performed the UV continuum subtraction procedure using CASA's *uvcontsub* task. This task estimates the UV continuum emission by fitting a n degree polynomial to the (u, v) data, which consists of a real and imaginary part. We did a plot of the integrated spectrum of the science target in CASA's *plotms* task in order to find the channels that have to be avoided in the UV continuum subtraction. Since we had to calculate the fit for line-free emission, we specified the spectral windows and channels that had to be left out with the respective task parameters for all seven visibilities. We set the polynomial fit to the 0-th order, i.e. a constant line. Due to the positive definite nature of the amplitude, we did not expect the line-free channels to go entirely to zero. They should just average to a very small value that reflects the noise.

5.3.2 Spectral line imaging

Following the UV continuum subtraction is the spectral line imaging of the visibilities. Spectral line imaging in CASA is handled by the *tclean* task. This task is based on the CLEAN algorithm (Högbom 1974), which is the most known image reconstruction method for interferometric data. We will use this algorithm to reconstruct the most similar sky brightness distribution of the OMC-2 FIR 4 region to the true one. This will allow for the most accurate results for the subsequent kinematic analysis. The CLEAN algorithm is an iterative deconvolution technique designed to remove artifacts (sidelobes) from the dirty image. The algorithm operates in the following way:

[4] https://casaguides.nrao.edu/index.php/First_Look_at_Line_Imaging_CASA_6.5.4

- Identifies and isolates bright sources (peaks) in the dirty image
- Models each peak as a point source
- Subtracts the point source's dirty beam from the dirty image
- Repeats this process until the residual image is minimized

The basic CLEAN algorithm produces a "model" image by adding these isolated point sources. The residual image is then combined with the model to create a final image that more closely resembles the true sky brightness distribution.

The *tclean* task always starts with an initialization process. CASA reads in the visibility data and sets up the grid according to the specified imaging parameters, which are the image size, the cell size (angular resolution of each pixel), and the frequency channels. The dirty image is created by Fourier transforming the visibilities and is then corrected by the primary beam response to form a field-of-view-limited view of the sky. This dirty image shows the actual emission convolved with the dirty beam, which contains sidelobes because of the incomplete sampling. After initialization, *tclean* operates in a series of major and minor cycles. During the minor cycle, *tclean* performs the above-mentioned CLEAN steps until a user-defined stopping threshold (clean threshold) or iteration limit is reached. After a certain number of minor cycles, *tclean* enters a major cycle. Here, the visibilities of the model based on the current CLEAN model are predicted and compared with the observed visibilities. Then it updates the residual image using the difference between the observed and the model visibilities. Once the CLEAN process reaches a user-defined stopping point, the final image is generated. The output of *tclean* is not just the cleaned image, but also the model and residual images[5].

5.3.3 Data reduction

We got a total of seven visibility files from the ALMA helpdesk for the 2016.1.00681.S project. All seven visibilities had to be concatenated before applying the CLEAN deconvolution algorithm. We did this with the help of the *concat* task. Before that, we extracted in each visibility the field of OMC-2 FIR 4 and the spectral window around the N_2H^+(1-0) line in a separate visibility file (CASA *split* task). Also, we reduced the channels inside the corresponding spectral window to only 200, which comprise all the line emission with a bit of continuum, but not the rest of the continuum. We did this step to reduce the calculation times later on, since for a reliable cleaning, the maximum iteration number had to be set high at 150000 iterations. We set the spectral definition mode to "cube" because the objective is spectral line imaging and set the rest frequency to the central frequency of N_2H^+(1-0), which is 93.173 764 GHz. We calculated the starting channel parameter in velocity using the following formula:

$$v_{\text{start}} = v_{\text{system}} - \frac{n_{\text{channel}} \cdot v_{\text{width}}}{2}, \tag{5.1}$$

where v_{start} is the starting velocity, $v_{\text{system}} = 11.4\,\text{km}\,\text{s}^{-1}$ the system velocity (relative velocity of OMC-2 FIR 4 to the earth identified by the PI), $n_{\text{channel}} = 200$ the defined number of channels,

[5] https://casadocs.readthedocs.io/en/stable/api/tt/casatasks.imaging.tclean.html

and $v_{\text{width}} = 0.1964\,\text{km}\,\text{s}^{-1}$ the defined width of a channel. Initially, we chose the cell/pixel size to be a fifth of the restoring beam size of $1.8''$ (circular), because in Fontani et al. (2020) the ALMA images have a synthesized beam of $\sim 1.5'' \times 1.8''$. We set the gridder to standard, which is a prolate spheroid with 7×7 UV pixel support size. When it comes to the deconvolver algorithm, or minor cycle algorithm, we use an adapted version of Hogbom CLEAN (Högbom 1974). This specific version finds the location of the peak residual, then adds this delta function component to the model image, subtracts a scaled and shifted PSF of the same size as the image from regions where the two overlap, and repeats the whole process. We took a Briggs weighting (Briggs 1995) for cubes as a weighting scheme and tried multiple values for the Briggs weighting robustness parameter. Specifically, we tested three values for the robust parameter on cleaning of a single visibility:

- -2.0 (uniform weighting)
- +2.0 (natural weighting)
- 0.5 (standard weighting)

As mentioned above, we tested the robustness parameter in CLEAN using uniform, natural, and standard weighting. One thing to note is that we performed the cleaning on only one of the seven visibilities.

5.3.4 Image quality assessment

It is highly important to assess the quality of the output images when interpreting and applying the methods that were used to obtain these (Pety et al. 2013). In our case, we tested the three different robust parameter values to see how much each parameter changes the final image's smoothness (sensitivity) and sharpness (resolution), where our goal is to find the one that has a good trade-off between the two qualities. To assess the quality of the three cleaned images, we used Plunkett et al. (2023) image quality assessment tools (IQA), as well as the Github page[6]. The goal of the IQA is to compare the differences in flux of a target image $I_\nu(x, y)$ with a reference image $R_\nu(x, y)$. In this case, we took the standard weighting image as a reference image, while the uniform and natural weighting images were taken as the target images. We did this because the standard parameter lies between the two other extreme parameters, allowing for a fair comparison of the three.

Ideally, continuum or low emission regions in the cube should be used to calculate the rms noise of the images, because these derive from instrumental noise, but should be excluded when doing the IQA. Hence, we need an assessment mask that includes a global intensity threshold to make the analysis easier. The assessment mask is defined as follows:

$$\text{AM}_\nu(x, y) = (3 \times \text{rms}_{\text{mask}}) \cdot \frac{1}{\text{PB}_\nu(x, y)} \cdot \frac{\theta_R}{\theta_0}, \tag{5.2}$$

where $\text{AM}_\nu(x, y)$ is the assessment mask, rms_{mask} is the noise level outside the source of the target image, $\text{PB}_\nu(x, y)$ is the primary beam correction map, θ_R is the native beam size of the

[6]https://github.com/teuben/DataComb

reference image and θ_0 is the target image with native beam size. The parameters x and y indicate that the mask is calculated pixel by pixel, while ν indicates that it is for single images or image cubes. The term $3 \times \text{rms}_{\text{mask}}$ is the mask threshold, which ensures the exclusion of noise for the latter IQA. The considerations that are made to get Eq. 5.2 are discussed in Plunkett et al. (2023).

We must apply the assessment mask $\text{AM}_\nu(x, y)$ to both the reference and target image to perform the IQA. This means that we have to apply a primary beam cut to all three robust parameter images, convolve all to the same beam, and calculate the noise level for all three to have an appropriate comparison. The output of cleaning are not only the reconstructed image cubes, but also the primary beam pattern, the PSF pattern, the model image, the residual, the deconvolution mask, and the single-pixel image containing the sum of weights per plane. With the primary beam pattern, we corrected all three robust parameter images by the primary beam response. The task *impbcor* executes this by feeding the output image with the primary beam pattern. Furthermore, we applied a PB cutoff value of 0.6 to all three images to eliminate what is outside the corrected image for the PB response to a radius where the sensitivity drops to 60% of the maximum value in the pointing center. The sensitivity of the telescope is highest at the center of this beam (the pointing center) and decreases as one moves away from the center. This drop in sensitivity follows a pattern that is typically Gaussian-like (only in single pointings). Without correction, sources at the edges of the field of view appear dimmer than they really are because the antennas are less sensitive in those regions. This step is essential before applying any data combination technique of images, but in this case also because of the assessment mask. We covolved the three PB-corrected robust parameter images to equal beam sizes of $2''$ with the help of the *imsmooth* task. We chose this value because images can only be convolved to a worse resolution and all three images had different beam sizes ranging from $1.6''$ to $1.8''$. Also, choosing a "worser" resolution than the worst resolution image allows the images to be more robust against noise, which can negatively affect the IQA. Finally, we regridded the images spatially to a template image (imregrid task), in this case to the reference standard weighting image. These steps simplified the assessment mask to only the mask threshold. We then exported the images as FITS files to a Python environment. From there, we need to find the rms of the reference image. For the standard weighting image, we determined the off-source noise level to be 24 mJy. With the help of Eq. 5.2 we applied the assessment mask to all images.

The next step to complete the IQA analysis is to assess the flux recovered from a target image with respect to a reference image. In fact, the most common assessment of recovered flux is a parameter called image fidelity (Cornwell et al. 1993), but it has limitations when evaluating individual images in absolute terms (see the discussion in Plunkett et al. (2023)). Instead, we used the new assessment parameter from Plunkett et al. (2023), the so-called accuracy parameter (A-par), defined as:

$$\begin{gathered} A_\nu(x, y) = \frac{I_\nu(x, y) - R_\nu(x, y)}{|R_\nu(x, y)|}, \\ -\infty < A_\nu(x, y) < \infty. \end{gathered} \tag{5.3}$$

$A_\nu(x, y)$ is the accuracy parameter, $R_\nu(x, y)$ the reference image, and $I_\nu(x, y)$ the target image. The A-par values display the relative differences between the fluxes of $R_\nu(x, y)$ and $I_\nu(x, y)$, where the sign indicates whether the emission is underestimated ($A_\nu < 0$) or overestimated ($A_\nu > 0$). A distribution around 0 means that the target image is similar to the reference image and recovers pretty much all the flux.

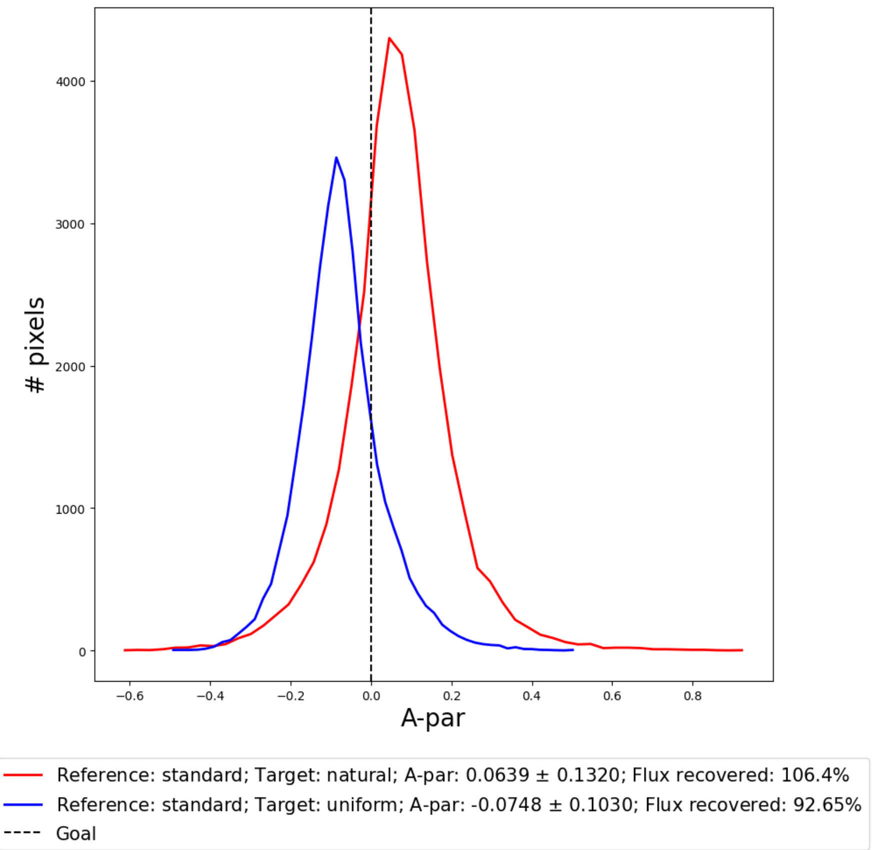

Figure 5.2: Comparison of the A-par distributions for the natural (red) and uniform (blue) weighting images on the standard weighting image. Histogram of A-par values with mean, standard derivative and recovered flux values in percent. Vertical black dashed-line indicates the zero goal mark.

Then, we calculated two A-par values pixel by pixel, having the standard weighting image as reference, while the natural and uniform weighting image as the target, respectively. Furthermore, we also calculated the mean with the standard derivative of the A-par and the recovered flux of the target with respect to the reference. We plotted the results in an A-par histogram (see Fig. 5.2). Both A-par histograms in Fig. 5.2 follow a Gaussian distribution, where the target uniform has a lower amplitude and is shifted slightly left of the goal mark ($-7.5\% \pm 10.3\%$ w.r.t. to the standard) with a flux recovery of 92.7% (underestimated flux), while the natural has a higher amplitude and is slightly shifted to the right of the goal mark ($6.4\% \pm 13.2\%$ w.r.t. to the standard) with a flux recovery of 106.4% (overestimated flux). The amplitude shifts (position and intensity deviation) are systematic biases introduced by the different weighting schemes due to how they sample spatial frequencies. The left shift of the uniform w.r.t. to the standard suggests a centroid displacement or suppression of extended emission in the dirty map. This aligns with the reconstructed uniform image, which has a higher angular resolution and looks sharper than the standard image. The underestimated flux might suggest that the uniform weighting likely misses extended emission because the long-baseline weighting suppresses low spatial frequencies. On the other hand, the right shift implies a boost in extended flux or noise "bleeding" into the structure. This aligns with the reconstructed natural image, which has a lower angular resolution and looks smoother than the standard image. The overestimated flux might suggest that the natural weighting likely includes noise or a slightly oversmooth structure, leading to artificial flux enhancement.

Ultimately, we chose the standard robust parameter because it is a balanced compromise between sensitivity and resolution. Natural weighting prioritizes sensitivity by giving more weight to short baselines, which correspond to large-scale structures when observing with an interferometer. This maximizes the signal-to-noise ratio (SNR) for faint, diffuse sources but sacrifices resolution and can lead to a "smeared" image with poorer angular resolution. Uniform weighting prioritizes resolution by giving equal weight to all baselines, emphasizing long baselines that capture finer details. Although this improves the angular resolution, it tends to reduce sensitivity, making the image noisier, especially for weak sources. The value of 0.5 offers good balance, providing reasonable angular resolution while maintaining relatively high sensitivity. This makes it ideal for observations where both resolution and sensitivity are important, which is indeed the case in this work.

5.3.5 N_2H^+(1-0) line imaging

At this point, we carried out the cleaning of all concatenated visibilities with the chosen robust value and the previously defined *tclean* parameters. Then, we PB-corrected the output image with a PB cut-off equal to 0.6 using the PB pattern image as a template. We performed the same procedure with only the concatenated 12-m array visibilities, in order to compare the two reconstructed image cubes with the image cube from Hacar et al. (2018) as a reference. This should confirm that by taking into account also the 7-m data, one should see improvements in sensitivity and recovered flux. The map of Hacar et al. (2018) was unsurprisingly the other chosen OMC-2 project, as it is the result of the combination of data from ALMA 12 m with data from IRAM 30-m. Data combination allows one to merge the high-resolution, small-scale information from an interferometer with the large-scale, diffuse information from a single-dish telescope. This process recovers missing flux and provides a more complete representation of the observed sky. This is the reason why the map of Hacar et al. (2018) is chosen as a reference, because it should roughly resemble the "true" sky emission distribution coming from OMC-2 FIR 4. Analogously to the case of the robust parameter, we carried out an IQA. Before exporting the images into FITS files, we convolved the synthesized beam of 1.8″ to a beam of 4.5″, which is the synthesized beam of the reference map. Then, we reprojected the images to the smallest one, which is the 12-m image. After cleaning, one would expect that both images would have the same size, but it turned out that the 12-m + 7-m image is larger than the 12-m image. When performing the deconvolution on just the 7-m visibilities, one can see that the resulting image has the same size as the 12-m + 7-m image. This explains the size discrepancy of the two images, but it does not explain why there is such a discrepancy between the reconstructed 12-m and 7-m images. Unfortunately, after multiple attempts to identify the error by changing *tclean* parameters and visibility concatenation, the reason for the size difference could not be found.

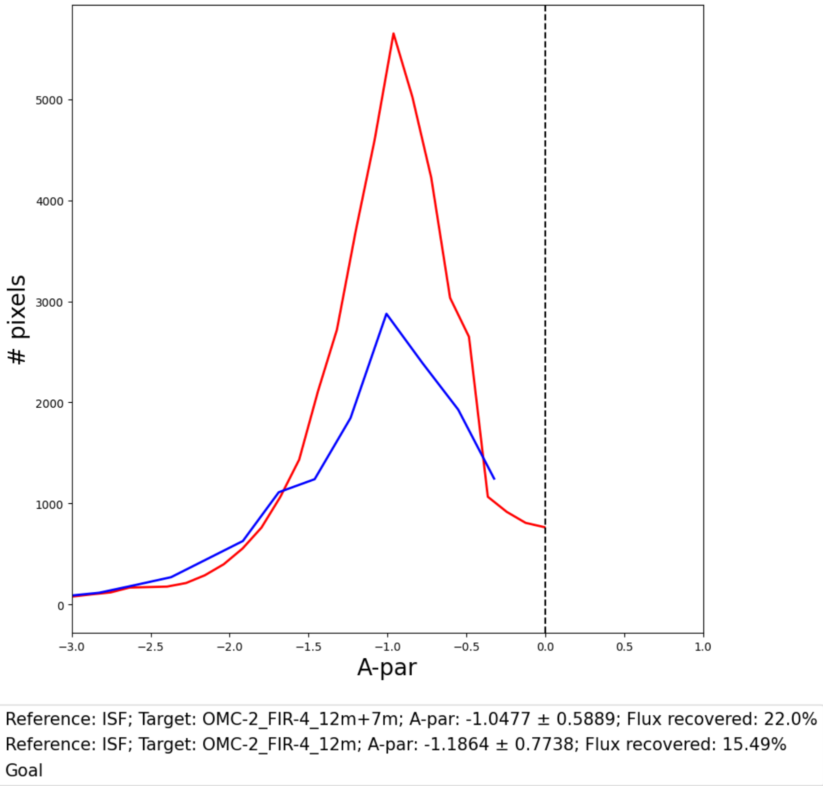

Figure 5.3: Comparison of the A-par distributions for the 12-m + 7-m (red) and 12-m (blue) images on the re-projected ISF image. Histogram of A-par values with mean, standard derivative and recovered flux values in percent. Vertical black dashed-line indicates the zero goal mark.

The A-par of both images was then calculated and plotted as an A-par histogram (see Fig. 5.3). Both A-par distributions in Fig. 5.3 are shifted left of the target mark, where the 12-m + 7-m image has a spike with a higher amplitude ($-104.8\% \pm 58.9\%$ w.r.t. to the ISF image) and a flux recovery of 22.0% (underestimated flux), while the 12-m image has a spike with a lower amplitude ($-118.6\% \pm 77.4\%$ w.r.t. to the ISF image) and a flux recovery of 15.5% (underestimated flux). The difference in amplitude derives from the extent of the image, but the difference in the recovered flux and mean of the distribution comes from the fact that the 12-m + 7-m image was reconstructed from a more complete (u, v) plane coverage. However, this plot does not prove that combining the 12-m and 7-m array observations of the 2016.1.00681.S project will improve the recovery of flux and the overall quality of the reconstructed image, because the A-par value is similar within errors.

5.4 Data combination

Combining data from different telescopes or configurations is critically important in radio astronomy for several reasons, mainly related to solving different spatial scales and improving image quality. Data combination allows one to merge the high-resolution, small-scale information from an interferometer with the large-scale, diffuse information from a single-dish telescope. This process recovers missing flux and provides a more complete representation of the observed sky. Combining single-dish data with interferometric data fills in the missing (u, v) coverage, providing a more accurate Fourier inversion and producing a cleaner and more reliable image. This improves image fidelity and dynamic range, allowing astronomers to detect both faint diffuse emission and bright compact sources simultaneously without significant imaging artifacts. By combining single-dish and interferometric data, the total flux density is better preserved. This is particularly important for scientific studies where absolute flux measurements are critical.

To improve sensitivity and maintain the high angular resolution of the reconstructed OMC-2 FIR 4 image, we have to combine this image with the lower-resolution image from Hacar et al. (2018), which is more sensitive to most spatial scales. The first data combination method investigated is the renowned Feather algorithm (McMullin et al. 2007). This algorithm takes the low-resolution image and regrids it spatially and spectrally to the high-resolution image. Then a FT is applied on both images, so the next calculations are done in the (u, v) plane. In order to account for different beam sizes, the FT'ed low-resolution image is scaled by the ratio of clean beams (CBs) $\mathrm{CB}_{\text{hi-res}}/\mathrm{CB}_{\text{low-res}}$. Next, it combines the images in the (u, v) plane (Fourier space) by weighting them according to the spatial frequencies of the response of each telescope. Lastly, an inverse FT is performed on the combined data, which brings them back to the image plane (Plunkett et al. 2023). Further discussion of the Feather method can be found in Cotton (2017). We performed the Feather combination by inputting the low-resolution ISF image, which we spectrally regridded to the FIR 4 image, with the high-resolution PB-corrected reconstructed 12-m + 7-m FIR 4 image in CASA's *feather* task.

We tested the quality of the output image in an IQA by calculating and plotting its A-par over all pixels as a histogram (see Fig. 5.4). The A-par distribution lies pretty much on the goal mark ($-2.4\% \pm 9.1\%$ w.r.t. to the ISF image) and has a flux recovery of 98.4%, which is almost the whole flux of the reference. Methods like Feather demonstrate that data combination is essential to resolve different spatial scales and improve image quality to obtain more complete, scientifically valuable data.

The other investigated data combination technique is the Model-assisted CLEAN plus Feather method (MACF). MACF, like Feather, uses *feather* to combine the high-resolution interferometric image with the low-resolution SD image. However, the generated interferometric image does not derive from just the previously defined deconvolution parameters. In *tclean* the startmodel parameter is added by inserting the low-resolution (SD) image in units of Janskys per pixel instead of Janskys per beam. The benefit of cleaning with a SD image is that it contains reliable large-scale information (extended emission), giving the algorithm a better initial estimate of the underlying structure. One thing to note is that the short-spacing flux in interferometric observations is not constrained by the algorithm, thus making the reconstructed image just an intermediate image. The application of the MACF algorithm can be found in the following

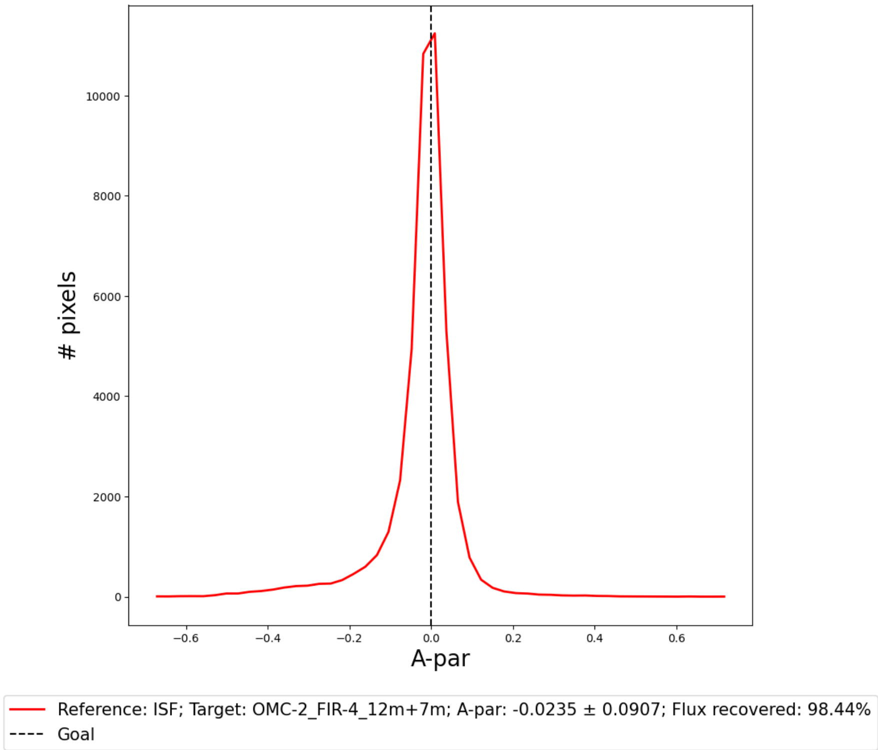

Figure 5.4: Comparison of the A-par distribution for the feathered 12-m + 7-m image with ISF image (red) on the re-projected ISF image. Histogram of A-par values with mean, standard derivative and recovered flux values in percent. Vertical black dashed-line indicates the zero goal mark.

recent studies (Dirienzo et al. 2015; Kauffmann et al. 2017; Hacar et al. 2018). We had to first modify the ISF image cube, which in this case is the startmodel image, before running *tclean*. Specifically, we had to regrid the image spatially and spectrally to the interferometric data and convert it from Jy/beam to Jy/pix. Moreover, we added an artificial Stoke axis in the exact axis order of the FIR 4 data. With these changes, the deconvolution with the startmodel successfully produced the clean image of FIR 4. After the PB correction, the combination of low-resolution image and high-resolution image is analogous to the Feather method.

As in the Feather case, we tested the quality of the output image in an IQA by calculating and plotting its A-par over all pixels as a histogram (see Fig. 5.5). The A-par distribution lies pretty much on the goal mark (0.2% ± 8.0% w.r.t. to the ISF image) and has a flux recovery of 100.5%, which is minimally more than the whole flux of the reference. Therefore, MACF seems to be slightly better than Feather, although these differences are within 10% (Bonanomi et al. 2024). Recognizing the differences in the IQA of the two data combination methods, our obvious choice for the subsequent kinematic analysis is the MACF reconstructed image.

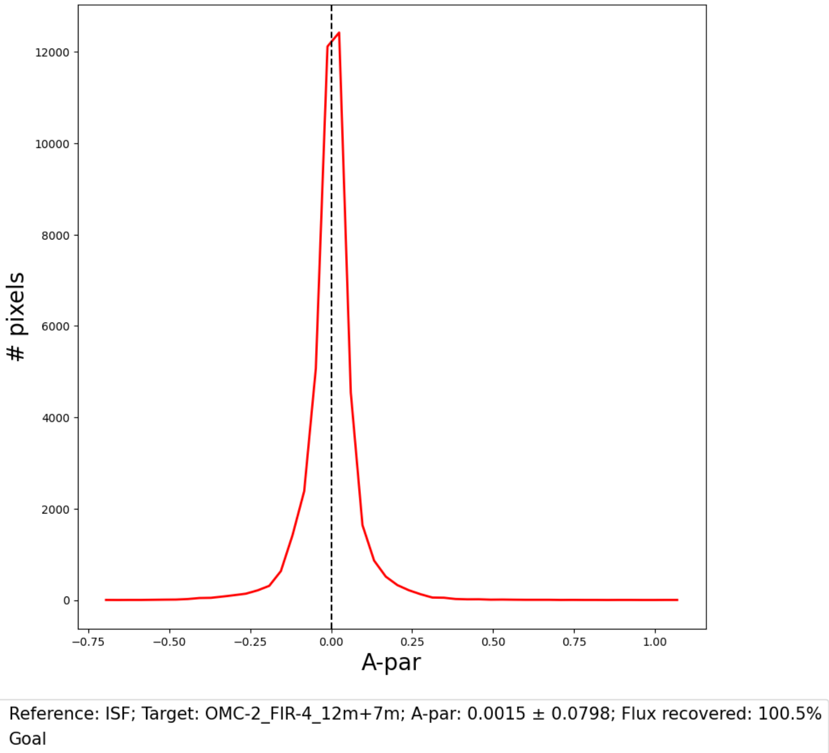

Figure 5.5: Comparison of the A-par distribution for the MACF image (red) on the re-projected ISF image. Histogram of A-par values with mean, standard derivative and recovered flux values in percent. Vertical black dashed-line indicates the zero goal mark.

5.5 Spectral line fitting

Spectral line fitting is the final step before beginning with the kinematic analysis, where we have to retrieve physical parameters such as the number of fitted N_2H^+(1-0) components, the coordinates (RA and Dec), the antenna temperature, the local standard of rest velocity, the full width half maximum, and the opacity from the fitting process that will be used in the kinematic analysis. The software used to this end is the Continuum and Line Analysis Single-dish Software (CLASS), which is part of the GILDAS[7] project. GILDAS is a collection of state-of-the-art software oriented toward (sub-)millimeter radioastronomical applications (either single-dish or interferometer).

Considering the fact that the spectral line in CLASS works on a pixel per pixel basis and the number of pixels of the MACF image is very high, due to the sampling rate of 5 pixels per synthesized beam, it is essential that we reduce the total number of pixels to shorten the fitting process to a realistic time scale. We achieved this by applying the Nyquist-Shannon sampling theorem (Nyquist 1928), which states that to accurately reconstruct a signal, it must be sampled

[7] http://www.iram.fr/IRAMFR/GILDAS

at least twice the highest frequency present in the signal (Nyquist rate). In other words, the cell/pixel size of the image has to be 0.9″, which is exactly half of the synthesized beam of the reconstructed MACF FITS map with a value of 1.8″. If the sampling rate is below the Nyquist rate, the higher-frequency components of the signal will be misrepresented as lower frequencies. This phenomenon, known as aliasing, can distort the spectral lines and introduce errors in the analysis. We reconstructed the MACF map with the Nyquist sampling technique.

We first converted the new MACF FITS file to a CLASS readable gdf file and created a CLASS source file. This step ensures compatibility with the CLASS data reduction software, which is specifically designed for spectral line analysis. Converting the FITS file to the gdf format and creating a CLASS source file allows for structured access to individual spectra and the application of specialized tools for such as baseline subtraction and line fitting. We used a Gaussian fit algorithm file (see Socci et al. (2024)) to automate the spectral fitting process and ensure consistency across all spectra. This allows for standardized detection and characterization of spectral lines, including their central velocity, linewidth, and peak intensity. By defining the fitting parameters (e.g., number of components, initial guesses, fitting ranges), it reduces user bias, improves reproducibility, and enables batch processing of large datasets efficiently. Moreover, a hyperfine data file of N_2H^+(1-0) was provided by Socci et al. (2024) that contains the relative positions and intensities of the components of the multiplet, as well as a file that overwrites the spectra already fitted. In the Gaussian fits algorithm file, we had to provide various parameters. We set the synthesized beam to 1.8″ and the box size length of each subfield to the cell size times five ($0.9'' \times 5$), which corresponds to 25 pixel for each subfield. Furthermore, we set the brightness temperature threshold to 0.05 K to eliminate weak signals and we set the spatial extents in x and y to $\pm 0.9'' \times 250$. After successfully setting these parameters, we invoked the algorithm in a CLASS environment, where the number of observations found is more than 9000 spectra. The algorithm starts scanning like a 5×5 pixel kernel over the image until it finds the first spectra. Once it finds the spectra, the program prompts one to fit the average subfield spectra. The first thing to look out for when seeing the spectra is to see if there is a single or multiple N_2H^+(1-0) component. N_2H^+(1-0) consist of seven total hyperfines, where the first is an isolated hyperfine, the next three are the main triplet hyperfines, and the last three are the secondary triplet hyperfines. Thus, the easiest way to determine the number of components is to look in the left part of the spectra where the isolated hyperfine lies. The amount of isolated hyperfines is then the number of components that one has to fit. The minimal distance between the centroids of two isolated hyperfines has to at least be the bigger FWHM out of the two. Keeping this in mind, we select the corresponding amount of components and then click around the peak/peaks of the central triplet/triplets. This creates a fit to the spectra with the selected number of components. Next, we minimize the residuals with a non-linear least-squares fitting process to optimize the line parameters for the selected components. Afterwards, we refine the fitting process further by running multiple iterations of the fitting algorithm. Finally, we display the fitted model/models on the observed spectrum. If the fit is satisfactory, we then save it through the write file and move on to the next subfield spectra (see Fig. 5.6).

The x-axis of the spectra is always in the frequency domain, but we display it in km s^{-1} because the spectral/data properties are known. However, if the fit is unsatisfactory, we need to review the selected parameters or the number of components, and we repeat the fitting process again.

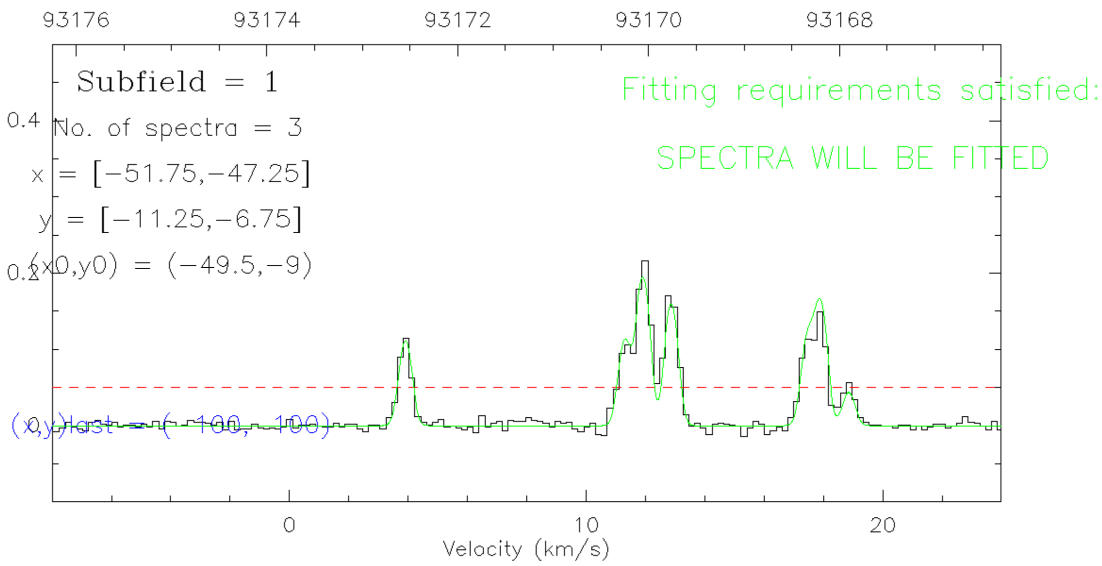

Figure 5.6: One component fitted spectra for subfield 1 of the MACF FITS file.

Alternatively, we can do this to single spectra of the subfield as well. In that case, we account for the baseline of the spectrum before applying the fitting process. In the spectral line fitting of the OMC-2 FIR 4 MACF map, we fitted a total of 9153 spectra, where ≈ 84% had one single N_2H^+(1-0) component, while ≈ 16% had two N_2H^+(1-0) components. Most of the subfield spectra that had one or two components were fairly straightforward to fit. The rest of the spectra were pretty tedious to fit because it was not always clear whether there is a double component or not, because of the closeness of the alleged two isolated components (could be self-absorption). Sometimes, the lines were really broad or had low amplitudes, which complicated our fitting process. In the end, we fitted the subfield spectra conservatively, which means that we fitted only one component if the second was not clearly visible. The algorithm outputs the final data table with all physical parameters and their errors once we fit all subfield spectra. These are the number of components, the coordinates (RA and Dec), the antenna temperature, the local standard of rest velocity, the full width half maximum, the opacity, and all the corresponding errors. We used the table values for all the upcoming kinematic analysis calculations.

6 Results

6.1 Comparison of MACF map with ISF map

A kinematic analysis allows us to probe the internal motions and dynamical structure of the fibers inside a molecular cloud, providing physical properties such as rotation, infall, outflows, turbulence, or gravitational collapse. This insight is essential to understand structure formation, mass assembly, stability, and evolution on scales from star-forming cores to giant molecular clouds (Dhabal et al. 2018). Comparison of our results with previous studies and incorporation of multiple tracers beyond N_2H^+ is essential for a physically complete interpretation. While N_2H^+ trace cold and dense gas, other lines like CO (outflow kinematics), SiO and CH_3OH (shock activity), and the dust continuum (total mass distribution) provide complementary views of the source. This multi-tracer approach allows us to disentangle the effects of dynamics, chemistry, and evolution, and to benchmark our findings against the broader context of star formation studies.

Comparison of a new reconstructed interferometric image with images from the literature is a valuable step in the scientific analysis of astronomical data because it helps verify whether the structures, features, and overall morphology seen in the new image are consistent with previous observations. If the new image shows significant deviations, it could indicate potential issues in the data processing or deconvolution steps. Furthermore, it acts as a quality check for the fidelity (or A-par) of the image to determine whether the reconstructed image accurately represents the true sky emission distribution. If the image shows morphological or kinematical features that do not appear in the previous literature, it could be a sign of a new discovery or an indication of an issue with the data. It is likely a new discovery if the new feature appears consistently across different imaging setups, is absent in prior studies due to technical limitations (e.g. resolution), aligns with physics, and is seen in other tracers or datasets. Newer telescopes or configurations, such as using ALMA or higher-resolution configurations, may reveal finer details or structures that were not visible in older observations. Therefore, comparing the image with the literature can help highlight improvements in spatial resolution, sensitivity, or dynamic range.

The first comparison of the newly reconstructed image through MACF is done with the total N_2H^+ integrated intensity ISF map of Hacar et al. (2018). We compare these two maps, because they both contain the OMC-2 FIR 4 region and have different angular resolutions ($\theta_{\mathrm{ISF}} = 4.5''$ & $\theta_{\mathrm{MACF}} = 1.8''$). The comparison provides critical insight into how emission structures evolve across spatial scales. It allows us to identify which features are truly compact and resolved only at high resolution and which are part of more extended emission detected at coarser resolution.

We first cropped the ISF image cube according to the MACF image cube. Then, we calculated the total integrated intensity map (moment 0) for both cubes, producing a single map for each image cube, where moment 0 is nothing more than the sum of the image fluxes along the spectral axis. This approach allows for a direct comparison of the spatial distribution and total

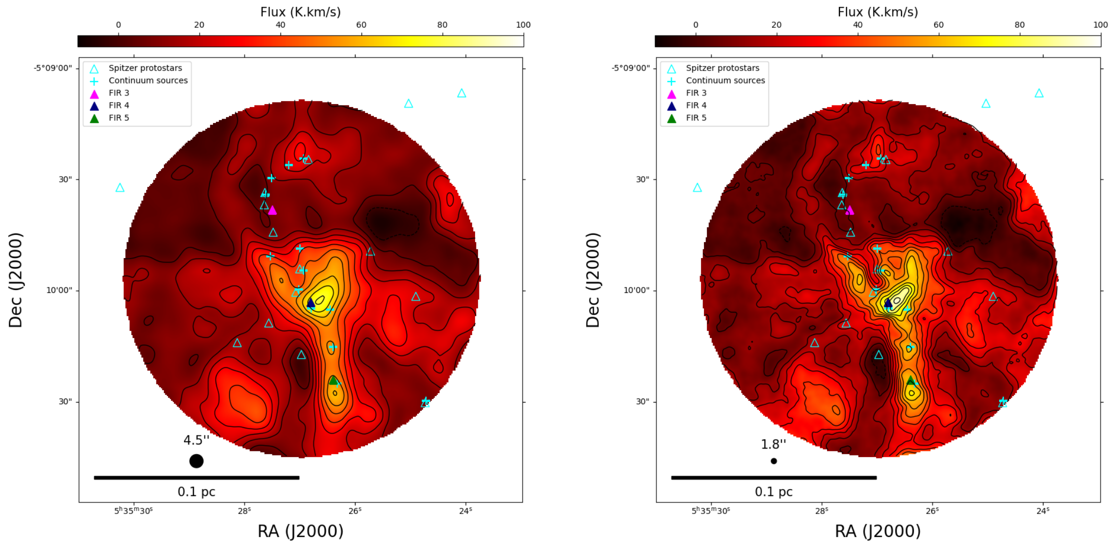

Figure 6.1: Comparison of ISF map vs. MACF map. (**Left**) Total integrated N_2H^+(1-0) intensity mosaic (combination of ALMA 12-m & IRAM 30-m) converted in $\mathrm{K\,km\,s^{-1}}$ of the ISF cropped to only OMC-2 FIR 4 (Hacar et al. 2018). (**Right**) Total integrated N_2H^+(1-0) intensity map (combination of ALMA 12-m + 7-m & Hacar et al. (2018)) converted in $\mathrm{K\,km\,s^{-1}}$ of OMC-2 FIR 4. For reference, the positions of FIR 4 (navy blue triangle), FIR 3 (magenta triangle), FIR 5 (green triangle) (Peterson & Megeath 2008) and both Spitzer protostars (cyan triangles; Megeath et al. (2012); Furlan et al. (2016)) plus continuum sources (cyan crosses; Teixeira et al. (2016); Kainulainen et al. (2017)) are shown in both panels. The corresponding beam sizes (black solid dot) are indicated in the lower left corner in comparison with a characteristic 0.1 pc scale (black bar).

flux of the line emission, independent of spectral resolution, and enables a robust evaluation of morphological differences and flux recovery across datasets. To account for the different synthesized beams, the image units were converted from Jy/beam to $\mathrm{K\,km\,s^{-1}}$ with the Gaussian beam assumption using the following formula (Cortes et al. 2023):

$$\left(\frac{T_\mathrm{B}}{1\,\mathrm{K}}\right) = \left(\frac{S_\nu}{1\,\mathrm{Jy}}\right)\left[13.6\left(\frac{300\,\mathrm{GHz}}{\nu}\right)^2\left(\frac{1''}{\theta_\mathrm{max}}\right)\left(\frac{1''}{\theta_\mathrm{min}}\right)\right], \quad (6.1)$$

where T_B is the brightness temperature in K, S_ν is the flux density in Jy/beam, ν is the observing frequency in GHz, θ_max the main beam axis in $''$, and θ_min the minor beam axis in $''$. After accounting for the velocity resolution of $0.196\,\mathrm{km\,s^{-1}}$, the images were plotted with 15 contours between the brightness temperatures of $-10\,\mathrm{K\,km\,s^{-1}}$ to $100\,\mathrm{K\,km\,s^{-1}}$ (see Fig. 6.1).

The new MACF map follows the same global N_2H^+(1-0) dense gas distribution of OMC-2 FIR 4 from the old ISF map. With an improved spatial resolution from $4.5''$ to $1.8''$ (factor of 2.5), the new map shows a more complex structure in the center of OMC-2 FIR 4. There seem to be three main fibers that trace the northern part of OMC-2 FIR 4, which all merge at the hub around FIR 4 (HOPS 108), and one main fiber that trace the southern part of OMC-2 FIR 4. These four dense gas fibers form a trident-like structure, which is not visible on the old map. Fibers contain protostars and continuum sources very well. The implication of improving the angular resolution is that one can resolve finer details and gain new insights into complex structures. This will lead to better estimates of mass, density, and temperature, as well as precise measurements of gas kinematics (see Sect. 6.3).

6.2 Comparison of MACF map with FIR 4 map of isolated F_1 = 0-1 hyperfine component

The second comparison of the newly reconstructed image through MACF is made with the total integrated intensity map of the hyperfine component N_2H^+(1-0) $F_1 = 0 - 1$ of Fontani et al. (2020). This component is well separated in velocity space from the blended hyperfine group and is typically optically thin, minimizing blending and radiative transfer effects. Focusing on this component allows us to compare the spatial distribution and integrated intensity of the emission across resolutions in a physically meaningful and unbiased way.

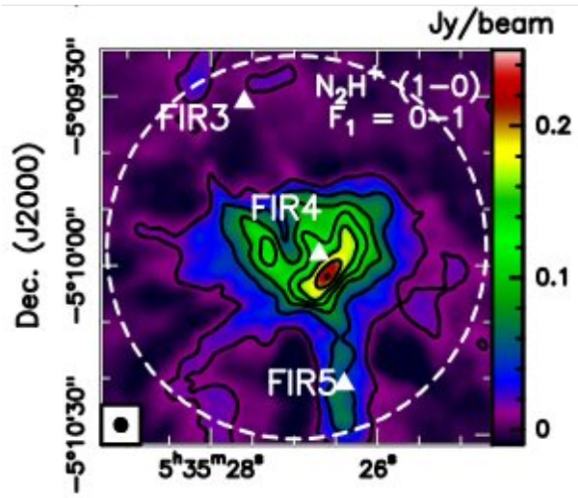

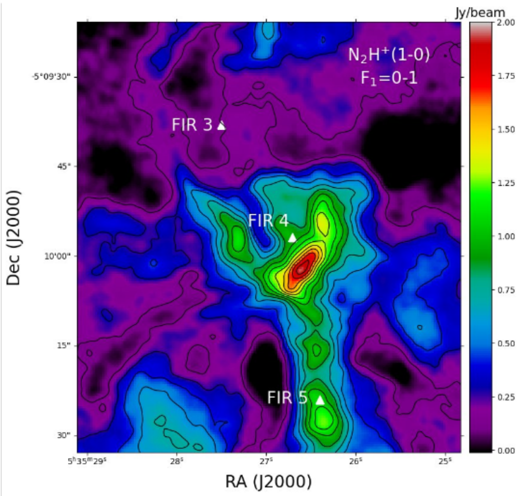

Figure 6.2: Comparison of FIR 4 map vs. MACF map. (**Left**) Total integrated intensity map over the hyperfine component N_2H^+(1-0)$F_1 = 0 - 1$ in Jansky per beam of OMC-2 FIR 4 from Fontani et al. (2020). (**Right**) Total integrated intensity map over the hyperfine component N_2H^+(1-0)$F_1 = 0 - 1$ in Jansky per beam of OMC-2 FIR 4 calculated from the MACF cube. For reference, the positions of FIR 4, FIR 3 and FIR 5 (white triangles) are shown in both panels.

For a correct comparison of the images, we calculated the new image's total integrated intensity map over the hyperfine component. The hyperfine component N_2H^+(1-0) $F_1 = 0 - 1$ is the isolated hyperfine of N_2H^+(1-0), meaning that we had to do the sum of the image fluxes just over the isolated component. In the case of the new image cube, we did the sum of velocities of $1.6\,\mathrm{km\,s^{-1}}$ to $5.5\,\mathrm{km\,s^{-1}}$, since this range covers the whole $F_1 = 0 - 1$ hyperfine component without any other hyperfine contributions. We plotted the resulting image in the same style as the FIR 4 image from Fontani et al. (2020) to make the differences easier to notice (see Fig. 6.2).

Similarly to the first comparison, the new MACF map traces the same global N_2H^+(1-0) isolated hyperfine dense gas distribution of OMC-2 FIR 4 from the old FIR 4 map. Both maps have the same angular resolution of 1.8″, so we made a comparison with respect to the flux in the images. The maximum flux in Fontani et al. (2020) map is equal to roughly 0.25 Jy/beam. In contrast, the maximum flux in the new MACF map is much higher at roughly 2 Jy/beam, which is a factor of 8 more than the old map. This huge difference can be attributed to the fact that the new map derived from the MACF data combination technique of the cleaned Fontani et al. (2020) map with the high sensitivity map of Hacar et al. (2018). This difference in the flux recovery factor of 8 is more or less true for the whole of FIR 4. This factor is pretty consistent with the IQA test performed between the 12m and ISF data with a factor of ≈ 6.6 (see Fig. 5.3). Fontani et al. (2020) did his map with only 12m data and the MACF map recovers the whole ISF flux, meaning that an IQA between 12m and MACF would yield approximately the same factor. The implication of improving the sensitivity is that one can detect fainter objects (uncover substructures) and trace the extended emission of a region, as well as reducing uncertainties of physical parameters of objects in that specific region.

6.3 Kinematic analysis

To investigate the internal dynamics of the dense gas in OMC-2 FIR 4, we performed a kinematic analysis using the N_2H^+(1–0) line. N_2H^+ is an ideal tracer for this purpose due to its stability in dense and cold environments and its well-resolved hyperfine structure, which allows precise determination of velocity and linewidth. This makes it especially useful for probing the quiescent core gas, revealing motions such as turbulence, velocity gradients, or possible infall (Hacar et al. 2017). In a region as complex as OMC-2 FIR 4, this analysis is key to understanding the role of dense gas dynamics in the ongoing star formation process.

6.3.1 Subsonic fibers in OMC-2 FIR 4

Before any calculations of kinematic analysis, we inspected the parameters of the line fitting results table in a histogram. These are the antenna temperature, the local standard of rest velocity, the full width half maximum, and the opacity. For the spectra with two components, we calculated the velocity separation. After a careful inspection, we rejected the following outliers:

- Full Width Half Maximum: FWHM > $2.5\,\mathrm{km\,s^{-1}}$
- Local Standard of Rest Velocity: $V_{\mathrm{LSR}} < 10\,\mathrm{km\,s^{-1}}$ & $V_{\mathrm{LSR}} > 13\,\mathrm{km\,s^{-1}}$
- Antenna Temperature: $T_{\mathrm{ant}} < 0.01$ Jy/beam
- Opacity: $\tau > 40$

Broad lines with FWHM > $2.5\,\mathrm{km\,s^{-1}}$ are highly unlikely in dense, cold cores like FIR 4. The systemic velocity of FIR 4 is well-established around $\sim 11.4\,\mathrm{km\,s^{-1}}$. Deviations beyond $\approx \pm 1.5\,\mathrm{km\,s^{-1}}$ are inconsistent with known motions in the core. Antenna temperatures with $T_{\mathrm{ant}} < 0.01$ Jy/beam fall below the reliable detection threshold and may result in unreliable or spurious line fits. There were a few optical depths with $\tau > 40$ in the histogram, which were far to different from the rest, thus being rejected to avoid biasing the interpretation of line intensities and derived column densities. In conclusion, we based the rejection thresholds for each parameter on the physical plausibility of the values, the known characteristics of N_2H^+(1-0) emission in dense cores, and visual inspection of the histograms. This step ensured that only well-constrained and physically meaningful spectra were used for the kinematic analysis, reducing contamination from noise, artifacts, or unrelated velocity components.

The internal dynamical state of dense gas within the fibers can be assessed through the nonthermal velocity dispersion σ_{NT}, which isolates the contribution of nonthermal motions from the total observed linewidth. This parameter is crucial for determining the level of turbulent support against gravity and to characterize whether gas movements are subsonic, transonic, or supersonic (Hacar & Tafalla 2011). As such, σ_{NT} plays a fundamental role in the evaluation of the stability of fibers and their ability to undergo gravitational fragmentation or collapse. It depends on the measured line FWHM of the hyperfine fits ΔV and the kinetic temperature:

$$\sigma_{\mathrm{NT}} = \left[\left(\frac{\Delta V}{\sqrt{8\ln 2}}\right)^2 - \frac{k_B T_{\mathrm{K}}}{\mu(\mathrm{N_2H^+})}\right]^{1/2}. \tag{6.2}$$

The local thermal sound speed of H_2 is a critical parameter in assessing the dynamical state of dense gas, as it defines the level of thermal pressure support and sets the scale for gravitational stability (Hacar & Tafalla 2011). Because it depends only on the gas kinetic temperature, it provides a direct and reliable reference for comparison with nonthermal motions. It is defined as follows:

$$c_s(T_{\mathrm{K}}) = \sqrt{\frac{k_B T_{\mathrm{K}}}{\mu(\mathrm{H_2})}}. \tag{6.3}$$

The ratio of $\sigma_{\mathrm{NT}}/c_s(T_{\mathrm{K}})$ is known as the Mach number $\mathcal{M}$ and is a diagnostic tool for three types of gas motions:

- Subsonic: $\sigma_{\mathrm{NT}}/c_s(T_{\mathrm{K}}) \leq 1$
- Transonic: $1 < \sigma_{\mathrm{NT}}/c_s(T_{\mathrm{K}}) \leq 2$
- Supersonic: $\sigma_{\mathrm{NT}}/c_s(T_{\mathrm{K}}) > 2$

Mach number values of $\mathcal{M} \leq 1$ indicate subsonic motions where thermal pressure dominates, consistent with stable quiescent conditions. The transition to the transonic regime suggests a balance between thermal and turbulent support. The transonic regimes ($1 < \mathcal{M} \leq 2$) are slightly dominated by nonthermal motions such as flows induced by turbulence, infall, or shock. The supersonic regimes ($\mathcal{M} > 2$) are also dominated by nonthermal motions, but the turbulence, infalls, and shocks are much stronger than the transonic regime. Thus, the Mach number provides a direct handle on the physical processes that shape the structure and evolution of the dense gas.

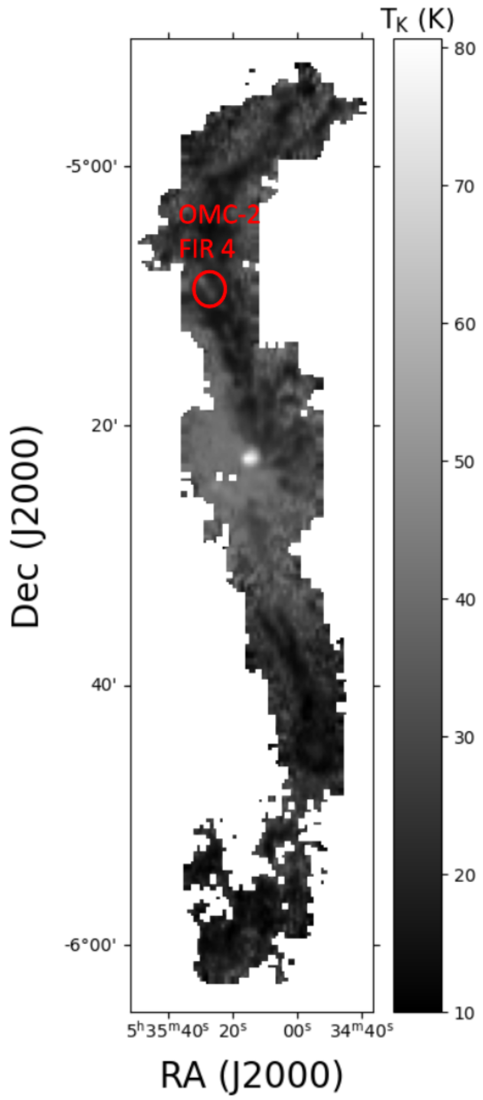

Figure 6.3: Kinetic temperature map of the ISF created through the HCN-to-HNC intensity ratio (Hacar et al. 2020). In red is circled the position of OMC-2 FIR 4.

To successfully calculate the Mach number, one needs to calculate ΔV and define T_K. The measured line FWHM of the hyperfine fits is calculated through the FWHM and the velocity separation for each pixel. In an environment without strong feedback effects, the kinetic temperature of the dense gas traced by N_2H^+ is low and uniform around $T_K \sim 10\,K$ (Myers & Benson 1983). In the case of the entire OMC-2 region, Friesen et al. (2017) derived the gas temperature through ammonia as (20.1 ± 2.2)K. Since there is stellar feedback in the FIR 4 region, the temperature varies a bit in that region. We used the ISF kinetic temperature map from the EMERGE dataverse[1] as a tool to determine the kinetic temperature of each pixel. In the ISF kinetic temperature map, OMC-2 FIR 4 has a mean kinetic temperature of $T_K \sim 25\,K$, which is 5 K higher than the result of Friesen et al. (2017). Hacar et al. (2020) created this kinetic temperature map using the HCN-to-HNC intensity ratio (see Fig. 6.3).

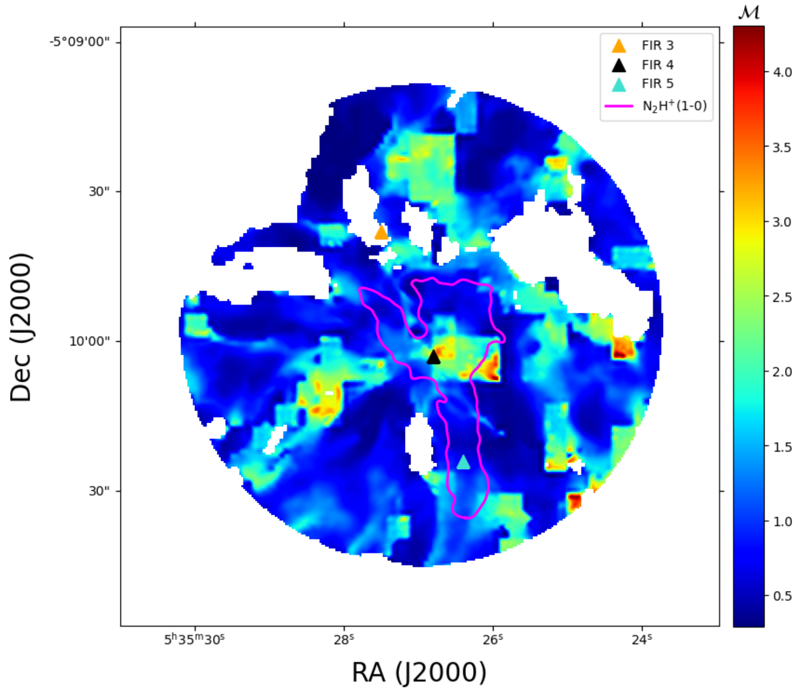

Figure 6.4: Mach number plot of the OMC-2 FIR 4 region. For reference, the positions of FIR 4 (black triangle), FIR 3 (orange triangle), FIR 5 (turquoise triangle) (Peterson & Megeath 2008) are shown. The N_2H^+ emission (magenta contour) for fluxes greater than $40\,K\,km\,s^{-1}$ is shown as well.

At this point, we calculated the nonthermal velocity along the line of sight and the local thermal sound speed of H_2 for each pixel. We then determined the Mach number for every pixel by the ratio of the two (see Fig. 6.4). In the $\mathcal{M}$ scatter map there are some zones with supersonic velocities sticking out, where 4.3 is the maximum Mach number value. Most of the gas around

[1]https://dataverse.harvard.edu/dataverse/EMERGE/

FIR 4 seems to be supersonic. The supersonic zones directly north, east, and south-west of FIR 4 partially trace the denser gas zones in N_2H^+. The sharp edges between supersonic and transonic/subsonic gas motions come from the spectral line fitting that took 5×5 pixels as a subfield.

	OMC-2 FIR 4
N_2H^+ fits	9153
$\langle T_K \rangle$ (K)	23.4
$\langle c_s(T_K) \rangle$ (km s^{-1})	0.310
$\langle \Delta V \rangle$ (km s^{-1})	0.922
$\langle \sigma_{NT} \rangle$ (km s^{-1})	0.379
$\langle \sigma_{NT}/c_s(T_K) \rangle$	1.22
$\sigma_{NT}/c_s(T_K) \leq 1$	48.9%
$1 < \sigma_{NT}/c_s(T_K) \leq 2$	35.0%
$\sigma_{NT}/c_s(T_K) > 2$	16.1%

Table 6.1: Table of statistical dense gas properties.

We calculated the average density gas properties by averaging the values of all pixels for each property. The mean kinetic temperature has a value of 23.4 K and with this we determined that the mean sound speed is 0.310 km s^{-1}. On the other hand, we determined that the mean nonthermal velocity dispersion along the line of sight is 0.379 km s^{-1}, while the average Mach number of 1.22 lies in the transonic gas motion range. Most of the OMC-2 FIR 4 region shows subsonic (~ 49%) and transonic (~ 35%) velocity dispersions, while only a small portion exhibits supersonic (~ 16%) velocity dispersions (see Tab. 6.1). This means that more or less half of the dense gas within the OMC-2 FIR 4 region is quiescent, while the other half is turbulent. Chahine et al. (2022) finds that the fibers in OMC-2 FIR 4 have typical Mach number values ranging from ~ 1 to 3.3, implying the presence of transonic and supersonic motions. These values are consistent with ours, but there is no comment or map explaining the distribution of these values and whether there are subsonic components.

6.3.2 Mass distribution in OMC-2 FIR 4

Another important factor in fiber analysis is how the mass is distributed within OMC-2 FIR 4. This can be described by the total $N(H_2)$ column density, which depends on the total integrated intensity (moment-0) of N_2H^+(1-0) and the kinetic temperature. The formulation in Hacar et al. (2018) comes from an empirical linear correlation between the observed single-dish N_2H^+ intensities (Hacar et al. 2017), normalized by the local gas kinetic temperature T_K (Friesen et al. 2017), and the total (gas + dust) column densities $N(H_2)$ derived in previous Hershel-Planck measurements (Lombardi et al. 2014) for the ISF:

$$N(H_2)\,[\mathrm{cm}^{-2}] = 67.4 \times 10^{21} \cdot \left(\frac{I(N_2H^+)\,[\mathrm{K\,km\,s^{-1}}]}{T_K\,[\mathrm{K}]} \right). \tag{6.4}$$

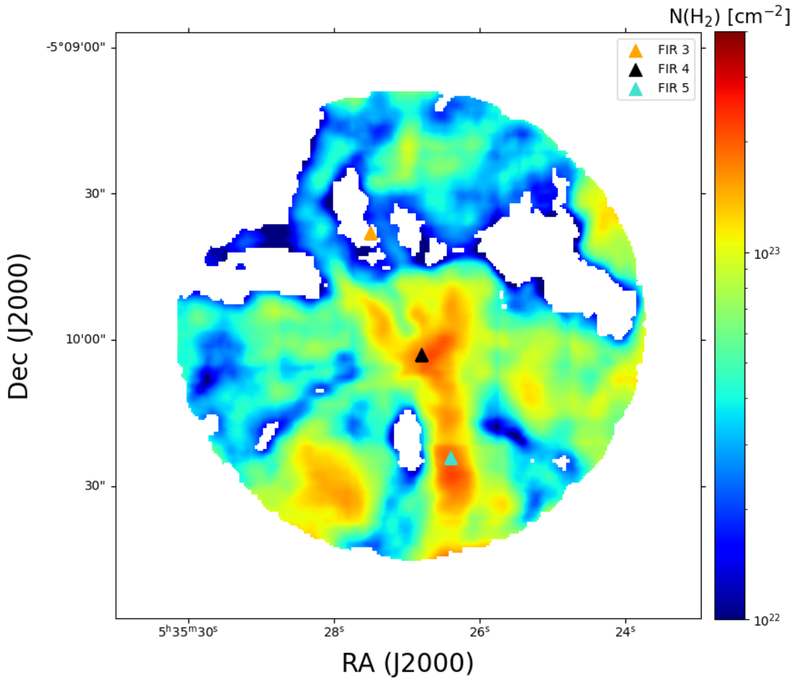

Figure 6.5: Column Density plot of the OMC-2 FIR 4 region. For reference, the positions of FIR 4 (black triangle), FIR 3 (orange triangle), FIR 5 (turquoise triangle) (Peterson & Megeath 2008) are shown.

We calculated the total $N(H_2)$ column density for every pixel using the moment-0 and kinetic temperature maps of OMC-2 FIR 4 (see Fig. 6.5). The $N(H_2)$ map is almost identical to the moment-0 map, since the latter was used for its calculation, and the temperature map is more or less homogeneous in OMC-2 FIR 4 (see Fig. 6.3). The column density in OMC-2 FIR 4 reaches values up to 2.22×10^{23} cm^{-2} and pretty much all of the densest material with $N(H_2) > 10^{23}$ cm^{-2} is contained in the trident fiber structure, consistent with the $N(H_2)$ column densities derived by Schuller et al. (2021). We estimated the total H_2 gas mass for $N(H_2) > 10^{23}$ cm^{-2} by the sum of column densities in pixels with that condition and got a value of $M(H_2) \approx 56\,M_\odot$.

6.3.3 Gravitational collapse in OMC-2 FIR 4?

The just-mentioned trident structure raised the suspicion that the structure formed through a gravitational collapse. Such a geometry is commonly interpreted as evidence of inflow motions channeled by filamentary structures, where gas is being accreted onto a denser hub or spine (Schneider et al. 2012). This is consistent with predictions from numerical simulations of gravitational collapse, where the filamentary substructure develops and feeds mass into central potential wells (Hoemann et al. 2024). We tried to confirm this suspicion by calculating the virial mass of the trident structure and comparing it with the total calculated H_2 mass derived from the

H_2 column density. The virial mass is given by (Kauffmann et al. 2013):

$$M_{\rm vir} = \frac{5\sigma_v^2 R}{G}, \tag{6.5}$$

where σ_v is the velocity dispersion and R is the radius of the cloud fragment. We determined that the virial mass is $M_{\rm vir} \approx 12\,{\rm M}_\odot$, which means that the total H_2 mass is 4.6 times higher than the virial mass of the trident. The virial parameter ($\alpha = \frac{M_{\rm vir}}{M(H_2)}$) is approximately 0.2, where $\alpha < 2$ implies that the cloud is likely to collapse (Kauffmann et al. 2013).

To investigate such a hypothesis, the right ascension was plotted against the N_2H^+(1-0) line velocity centroid ($V_{\rm LSR}$). This approach isolates the velocity structure along the longitudinal axis of the main filament, enabling us to detect coherent velocity gradients or converging motions indicative of inflow. In gravitational collapse scenarios, such systematic gradients, particularly if symmetric, are expected as gas flows along filamentary arms into a central dense region (Hoemann et al. 2024). Two asymptotic curves that are point mirrored around FIR 4 mimic one blueshifted and one redshifted flow with respect to the FIR 4 center. We used these for the subsequent analysis. If it is a gravitational collapse then one should see the following relation in the distance against l.o.s. velocity $V_{\rm LSR}$:

$$V_{\rm LSR}(p) = V_{\rm sys,0} + V_{\rm infall}(p) \cdot \cos(\alpha), \tag{6.6}$$

where p is the impact parameter, $V_{\rm sys,0}$ is the initial systemic velocity and $V_{\rm infall}(p) = -\sqrt{\frac{2GM}{R}} = -\sqrt{\frac{2GM}{p/\sin(\alpha)}}$ is the infall velocity (assumed to be free-fall) in a potential of a mass M as a function of the distance R to its center, with α describing the orientation angle of these infalling motions with respect to the line of sight (Hacar et al. 2017). In a gravitational collapse scenario, the gas is expected to accelerate toward a central mass, following a free-fall velocity profile. However, since we observe only the projected position p and the velocity of the line of sight, we must account for the geometric projection of the motion onto our line of sight, introducing the inclination angle α. Observing such a trend in the data would provide strong evidence that the gas is indeed collapsing under gravity toward a common center (Hacar et al. 2017). Thus, the observed velocities should have an inverse square root dependence ($p^{-1/2}$) with respect to the gravitational center. The inverse square-root dependence of velocity with projected distance arises under the assumption of free-fall collapse toward a central point-like mass. It assumes that the observed line-of-sight velocities are direct projections of the infall motion and that the geometry and mass distribution are relatively simple. In real star-forming regions, however, deviations from this profile may arise due to distributed mass, turbulence, magnetic fields, or overlapping kinematic components. Therefore, while such a relation provides a useful first-order diagnostic of gravitational collapse, it must be interpreted with caution and in conjunction with complementary spatial and spectral information.

We plotted the blueshifted and redshifted velocity curves extracted from the radial velocity cut in right ascension as a function of the distance to FIR 4 and could not find a $p^{-1/2}$ dependence but rather a p^{β} dependence with $\beta > 1$ (see Fig. 6.6). Since the observed velocity profiles are dependent on a $\beta > 1$, this would in principle describe an outflow. The chosen outflow model is a modified version of the Hubble flow (Davis & Peebles 1983), which we define as follows:

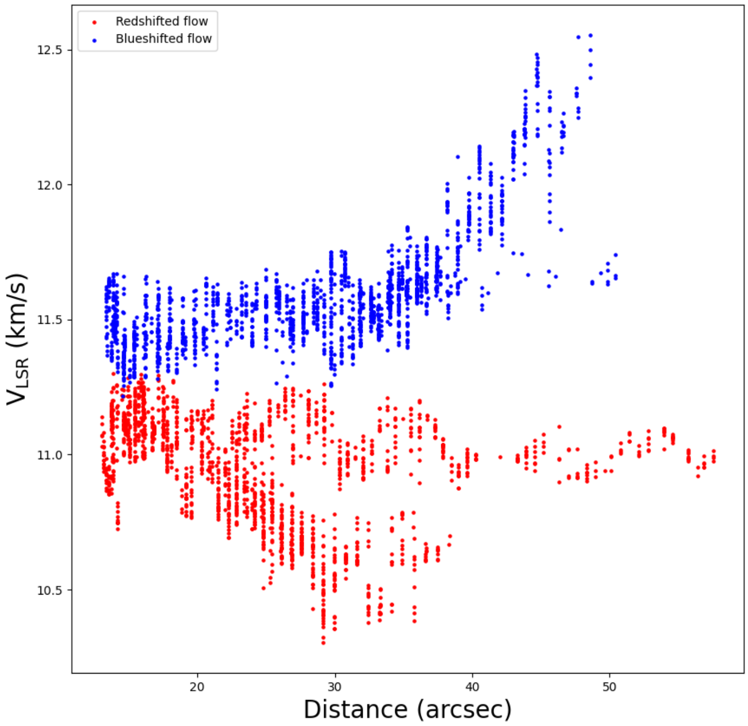

Figure 6.6: Blueshifted (blue) and redshifted (red) velocity curves extracted from the radial velocity cut in right ascension as a function of the distance to FIR 4.

$$V_{LSR}(p) = V_{sys,0} + h_0 \cdot \left(\frac{p}{\sin(\alpha)}\right)^{\beta}, \tag{6.7}$$

where h_0 is the Hubble flow constant and β is the outflow exponent. In dense molecular cloud environments, the expected value of β in a Hubble flow configuration is two (Shu et al. 1991), while the two gas velocity structures are best fitted by a dependence of $\beta \sim 4$. Such a high dependence of the distance w.r.t. the observed velocity is nonphysical because doubling the distance would mean increasing the observed velocity by a factor of 16.

Both velocity structures were checked on a 3D position-position-velocity (ppv) plot to see whether there is a spatial correlation. The plot revealed that there are no clear spatial correlations on any of the two gas velocity structures. Moreover, the structure of this ppv plot is too complex and intricate to be described by simple models (see Fig. 6.7). This complex structure suggests that the region's dynamics might be influenced by a combination of turbulent motions, overlapping velocity components, and possible feedback from outflows. Such complexity is expected in clustered star-forming environments, where large-scale flows, fragmentation, and energetic feedback all contribute to the observed kinematics (see example of the L1287 cloud in Juárez et al. (2019)).

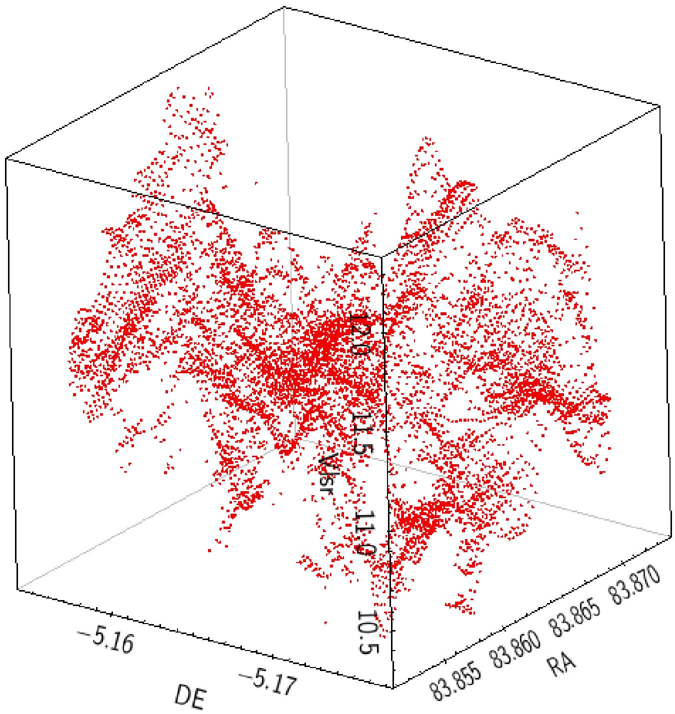

Figure 6.7: Position-position-velocity plot of the OMC-2 FIR 4 region.

6.4 Dust Continuum as protostar tracer

Characterizing a molecular cloud using only the N_2H^+ dense gas tracer provides valuable information about the cold, dense regions where star formation is actively taking place. However, using multiple tracers and continuum observations is essential for obtaining a complete and unbiased view of the cloud's physical and dynamical properties.

The dust continuum in OMC-2 FIR 4 directly traces the total gas + dust column density directly and is not affected by molecular depletion or chemical variations. It provides a census of dense cores that may lack strong molecular line emission. We took continuum data for OMC-2 FIR 4 from the 2016.1.00681.S project (Fontani et al. 2020) with a central frequency of 96.752 GHz. We plotted the continuum map with the Spitzer protostars (Furlan et al. 2016) and continuum sources (Teixeira et al. 2016; Kainulainen et al. 2017) (see Fig. 6.8). As expected, the continuum map traces almost all Spitzer protostars and continuum sources. All big continuum emission clumps are traced by a source, except for one north-east of FIR 4. The bulk emission of the continuum is in accordance with the bulk N_2H^+(1-0) distribution. Since this emission traces the total gas and dust column density of OMC-2 FIR 4 it indirectly also reveals the underlying mass distribution of that region.

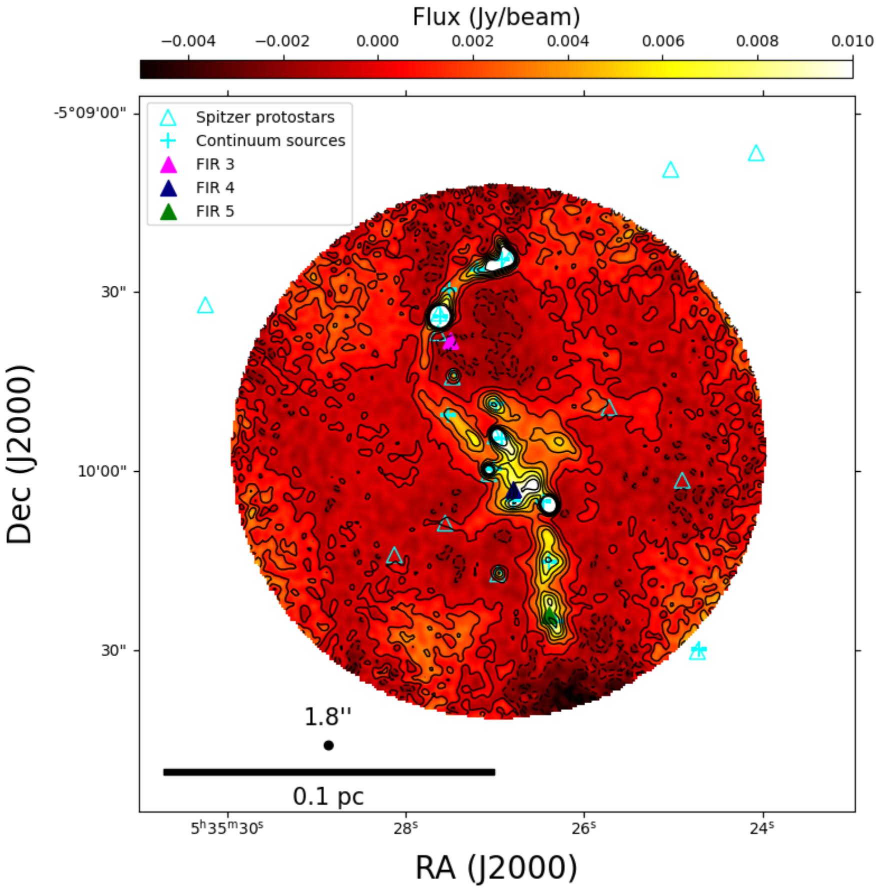

Figure 6.8: Continnum map of the 2016.1.00681.S project (Fontani et al. 2020) of OMC-2 FIR 4. For reference, the positions of FIR 4 (navy blue triangle), FIR 3 (magenta triangle), FIR 5 (green triangle) (Peterson & Megeath 2008) and both Spitzer protostars (cyan triangles; Megeath et al. (2012); Furlan et al. (2016)) plus continuum sources (cyan crosses; Teixeira et al. (2016); Kainulainen et al. (2017)) are shown. The corresponding beam sizes (black solid dot) are indicated in the lower left corner in comparison with a characteristic 0.1 pc scale (black bar).

6.5 CH_3OH & SiO as shock tracers

OMC-2 FIR 4 is a complex and active star-forming region where energetic feedback and gas dynamics play a significant role in shaping the environment (Sato et al. 2023). In addition to dense gas tracers like N_2H^+, we include CH_3OH and SiO as shock tracers to probe the kinematic and chemical signatures of protostellar feedback. CH_3OH is typically released into the gas phase from the grain mantles through low-speed shocks or heating, while SiO traces stronger shocks where the grain cores are disrupted (Coutens et al. 2017). The inclusion of these tracers allows us to characterize the spatial distribution and dynamics of shocked gas, complementing our view of the cold, quiescent material.

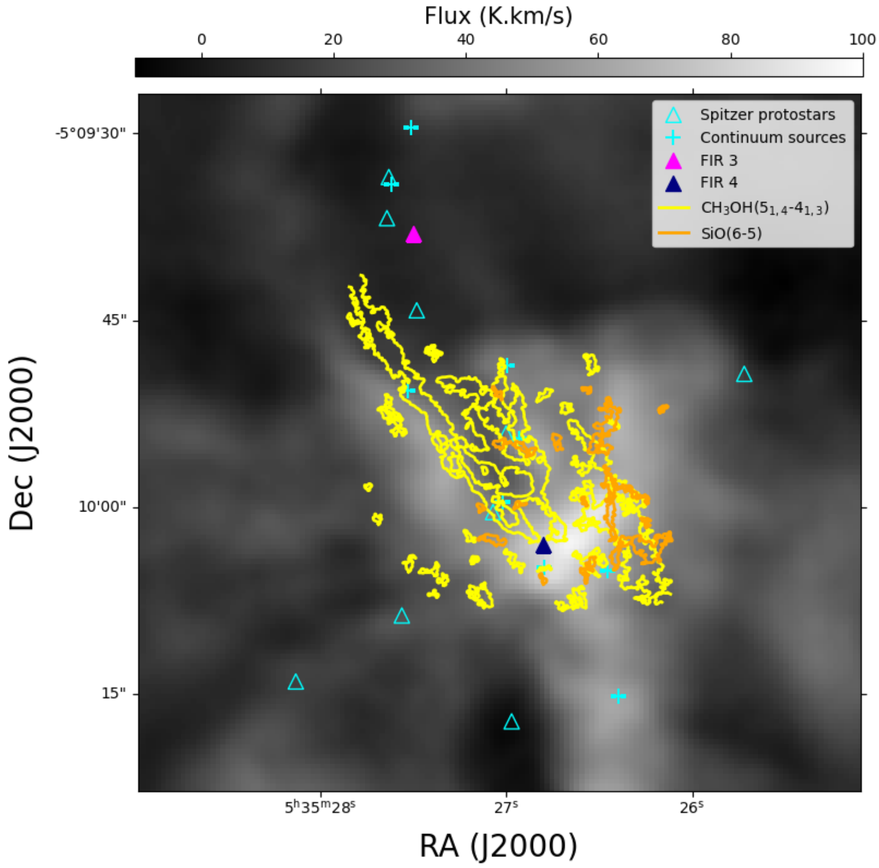

Figure 6.9: $CH_3OH(5_{1,4} - 4_{1,3})$ (yellow) and SiO(6-5) (orange) contours on MACF map. The defined contours are 6 K km s^{-1} and 12 K km s^{-1} for CH_3OH and SiO respectively. For reference, the positions of FIR 4 (navy blue triangle), FIR 3 (magenta triangle) (Peterson & Megeath 2008) and both Spitzer protostars (cyan triangles; Megeath et al. (2012); Furlan et al. (2016)) plus continuum sources (cyan crosses; Teixeira et al. (2016); Kainulainen et al. (2017)) are shown.

We retrieved data for $CH_3OH(5_{1,4} - 4_{1,3})$ and SiO(6-5) through the 2016.1.00376.S project (Chahine et al. 2022). We transformed the data for both tracers into integrated line intensity fluxes. To visualize the bulk emissions of both tracers with respect to the N_2H^+(1-0) map, we defined the contours according to it. We remove all noise and edge emission and define an emission threshold of 6 K km s^{-1} and 12 K km s^{-1} for $CH_3OH(5_{1,4} - 4_{1,3})$ and SiO(6-5), respectively. We then plotted these contours on the N_2H^+(1-0) map (see Fig. 6.9). While $CH_3OH(5_{1,4} - 4_{1,3})$ traces the west part of OMC-2 FIR 4, SiO(6-5) on the other hand traces the east part. There are two arc-shaped bow-shock features visible in SiO, where one of them is north-west (Arc 1) and the other one is west of FIR 4 (Arc 2), which derive from the collimated monopolar jet from VLA 15 (Chahine et al. 2022). The jet is traced by the main slim vertical contour of SiO(6-5) (see Fig. 6.9). The structure of the $CH_3OH(5_{1,4} - 4_{1,3})$ emission is aligned with Fiber 43 (see Fig. 3.2) from Hacar et al. (2018). The emission seems to come from FIR 3 towards FIR 4 and lies exactly between the left and middle fibers of the OMC-2 FIR 4 trident structure. FIR 3, located just north of FIR 4 in the OMC-2 region, is known to drive a powerful molecular outflow. Previous studies (Shimajiri et al. 2008; Chahine et al. 2022; Sato et al. 2023) have traced this outflow extending southward, intersecting the denser material surrounding FIR 4. As the outflow from FIR 3 encounters the dense gas envelope around FIR 4, it excavates a cavity in the molecular cloud. The presence of $CH_3OH(5_{1,4} - 4_{1,3})$ emission in this region suggests that the grain mantles are evaporated or sputtered by relatively slow shocks or heating in the cavity walls, releasing methanol into the gas phase. The edges of the cavity are delineated by enhanced SiO(6-5) emission that is commonly associated with stronger shocks when the grain cores are destroyed. The outer regions of the cavity experience more energetic impacts, likely as the outflow sweeps up and compresses the denser surrounding material.

6.6 CO as outflow gas tracers

To complement the dense gas tracer N_2H^+, we also include CO as a key tracer of the outflow activity and the extended gas kinematics in OMC-2 FIR 4. CO is particularly effective in revealing large-scale, high-velocity structures such as molecular outflows, which are not captured by N_2H^+ due to its focus on cold, quiescent, and dense regions. This is because CO forms rapidly after shocks through the high abundance in C and O (Tafalla et al. 2010).

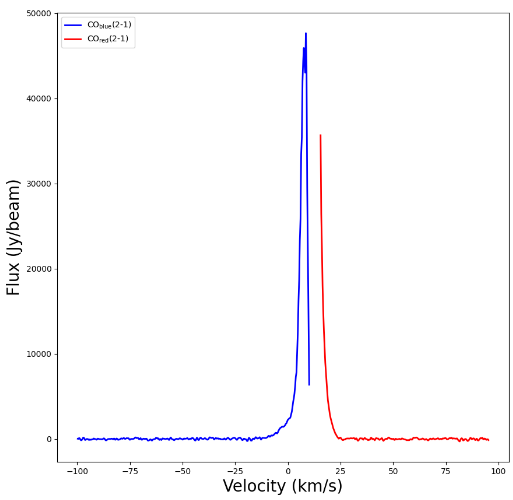

Figure 6.10: CO(2-1) blueshifted (blue) and CO(2-1) redshifted (red) spectrum of OMC-2 FIR 4. The defined velocity ranges are $-100\,\mathrm{km\,s^{-1}}$ to $10\,\mathrm{km\,s^{-1}}$ and $15\,\mathrm{km\,s^{-1}}$ to $95\,\mathrm{km\,s^{-1}}$ for CO(2-1) blueshifted and CO(2-1) redshifted respectively.

Outflows are readily identified via broad, high-velocity line wings in CO spectra, corresponding to gas accelerated by protostellar jets (Bjerkeli et al. 2013). This combination provides a more complete picture of the interaction between dynamic feedback and core structure, allowing us to assess how outflows from nearby sources (e.g., FIR 3) may influence the morphology and evolution of FIR 4 (Shimajiri et al. 2008).

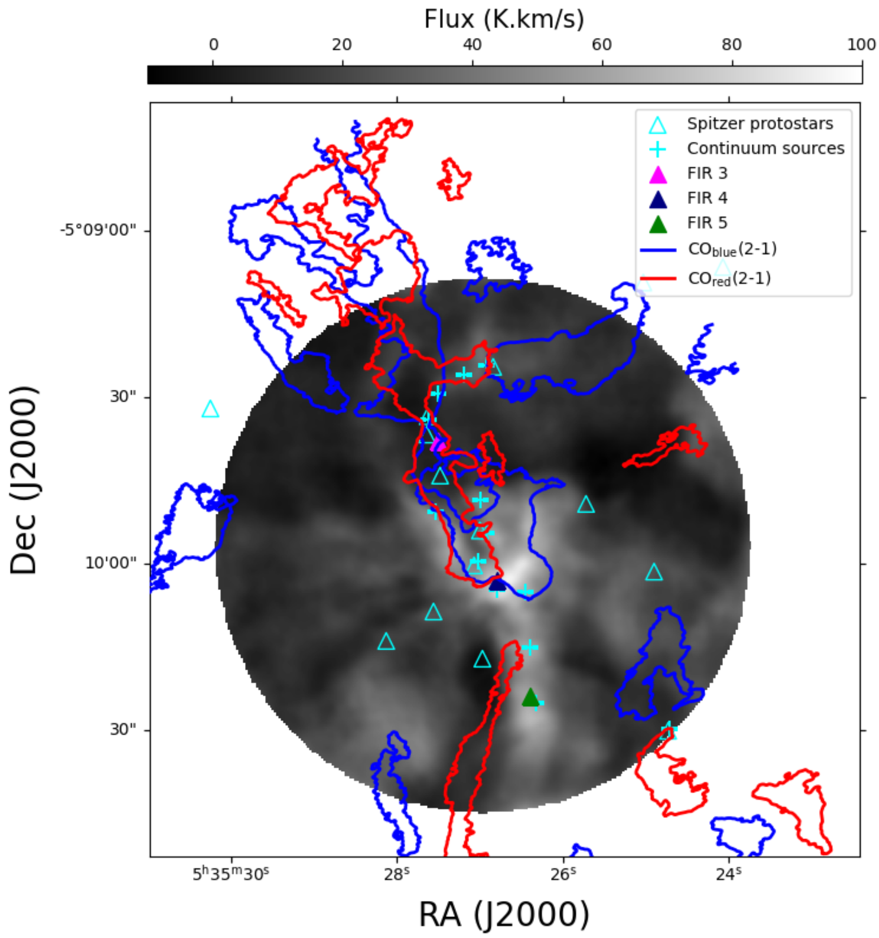

Figure 6.11: CO(2-1) blueshifted (blue) and CO(2-1) redshifted (red) contours on MACF map. The defined contours are 40 K km s^{-1} and 20 K km s^{-1} for CO(2-1) blueshifted and CO(2-1) redshifted respectively. For reference, the positions of FIR 4 (navy blue triangle), FIR 3 (magenta triangle), FIR 5 (green triangle) (Peterson & Megeath 2008) and both Spitzer protostars (cyan triangles; Megeath et al. (2012); Furlan et al. (2016)) plus continuum sources (cyan crosses; Teixeira et al. (2016); Kainulainen et al. (2017)) are shown.

We retrieved data for CO(2-1) through the 2017.1.01353 project (Sato et al. 2023). Since outflows appear as high-velocity blueshifted and redshifted wings in CO spectra (Tafalla et al.

2010), if the whole velocity range is integrated, the outflowing gas mixes with the quiescent cloud, making it harder to distinguish. This is why instead of making a single CO(2-1) integrated intensity map, a blueshifted and redshifted integrated intensity map were produced. We chose that the blueshifted integrated intensity map has velocity components ranging from $-100\,\mathrm{km\,s^{-1}}$ to $10\,\mathrm{km\,s^{-1}}$, while the redshifted integrated intensity map has velocity components ranging from $15\,\mathrm{km\,s^{-1}}$ to $95\,\mathrm{km\,s^{-1}}$, which we took from Sato et al. (2023) (see Fig. 6.10). After conversion of the maps into integrated line intensity fluxes, we defined the bulk emission contours as $40\,\mathrm{K\,km\,s^{-1}}$ and $20\,\mathrm{K\,km\,s^{-1}}$ for the blueshifted and redshifted map, respectively.

We plotted these contours against the N_2H^+(1-0) map for comparison (see Fig. 6.11). The blueshifted CO(2-1) emission has an hourglass shape with the bottleneck around FIR 3 and the axis parallel to Hacar et al. (2018) Fiber 43 (see Fig. 3.2). The lower part of the hourglass emission lies on top of the FIR 4 hub (Sato et al. 2023). On the other hand, the redshifted CO(2-1) emission is much narrower than the blueshifted emission but has the exact same orientation. This result is likely due to a combination of geometric inclination and environmental structure. The blueshifted emission may face the observer more directly and propagate into a less dense medium, allowing it to expand more freely. In contrast, the redshifted lobe may be partially obscured by the dense core or interact with denser ambient material, leading to a more compact and attenuated appearance (Ahmadi & Hacar 2023). In addition, the emission lies in the N_2H^+(1-0) cavity, where also $CH_3OH(5_{1,4} - 4_{1,3})$ was found. CO(2-1) emission can be also seen on the N_2H^+(1-0) cavity left of FIR 5, the stem of the trident structure. The feature may originate from the source at the top (see Fig. 6.11), but we did not find any literature to back this up.

6.7 Outflow-triggered star formation

Outflow-triggered star formation (Yokogawa et al. 2003; Shimajiri et al. 2008; Chahine et al. 2022; Sato et al. 2023) refers to the formation of new stars as a result of the influence of protostellar outflows (jets and winds) from already forming stars. The idea is that these outflows can compress nearby dense gas, triggering gravitational collapse in otherwise stable or marginally stable regions. There are several physical mechanisms that can be responsible for star formation triggered by outflow (Li et al. 2014):

- Shock compression: Outflows drive shocks into the surrounding molecular cloud, increasing density and pressure, and possibly exceeding the Jeans criterion for collapse

- Swept-up shells: As outflows sweep up material, they can create dense shells or filaments, where instabilities (e.g. gravitational) may trigger fragmentation and star formation

- Turbulence induction: Outflows stir the cloud, enhancing local turbulence. Although turbulence usually supports clouds against collapse, in some cases it can create dense, compressive modes that collapse into stars

- Interaction with pre-existing clumps: If a jet or wind slams into a marginally stable core, it might provide an extra boost to collapse

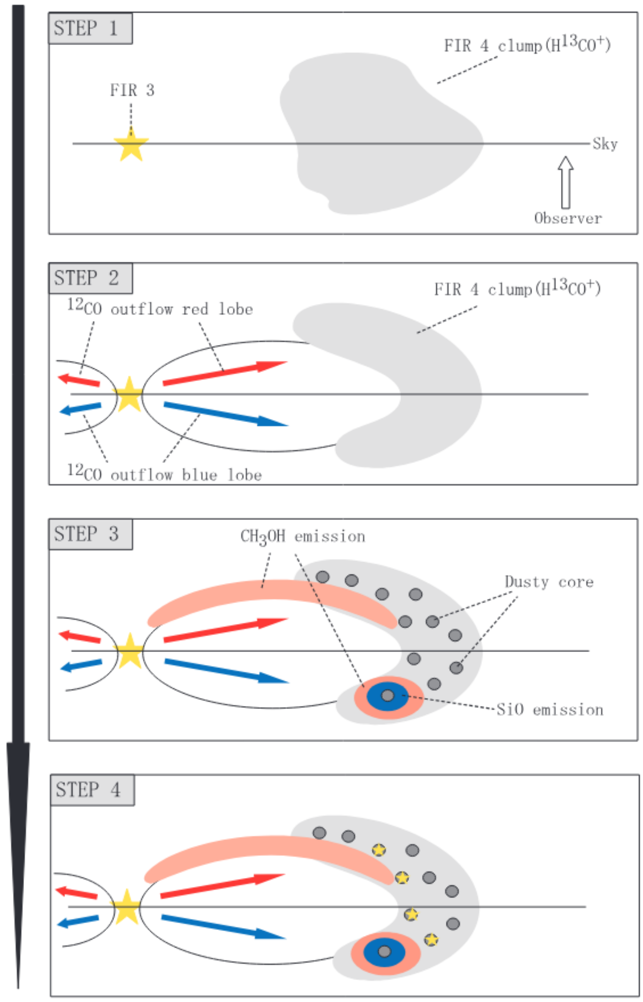

Figure 6.12: Schematic picture of the outflow-triggered star formation scenario in the FIR 4 region in four steps. The current stage of the FIR 4 region may be between step 3 and step 4. In these figures, horizontal lines show the plane of the sky and the observers are located at the bottom (Shimajiri et al. 2008).

In OMC-2 there is a suggested interaction between the molecular outflow driven by FIR 3 and the high-density clump of FIR 4 (Shimajiri et al. 2008; Sato et al. 2023). The observed CO(2-1) lines show a bipolar lobe-like distribution (blueshifted and redshifted) around FIR 3, with one lobe in the northwest direction and the other in the southeast direction toward FIR 4 (see Fig. 6.11). The extent of the southeast lobe ($\sim$ 0.1 pc) is substantially shorter than that of the northwest lobe ($\sim$ 0.2 pc). Shimajiri et al. (2008) suggests that the propagation of the southeast outflow is hampered by the FIR 4 clump material that is located at the end of that outflow. In other words, the FIR 4 clump is damming the outflow component. The interaction between the outflow and the FIR 4 clump gives rise to shocked regions seen in $CH_3OH(5_{1,4} - 4_{1,3})$ and SiO(6-5) (see Fig. 6.9). This is because such molecular lines are often observed in shocked regions that are caused by the interaction between an outflow and the dense gas (Avery & Chiao 1996; Bachiller et al. 2001). These morphological, kinematical and chemical evidence led Shimajiri et al. (2008) to set up the following outflow-triggered star formation scenario in FIR 4 (see Fig. 6.12):

- Step 1: FIR 3 was born and drove the outflow
- Step 2: The outflow driven by FIR 3 started interacting with FIR 4 clump
- Step 3: The interaction caused the fragmentation of FIR 4 clump into cores
- Step 4: These cores will form stars

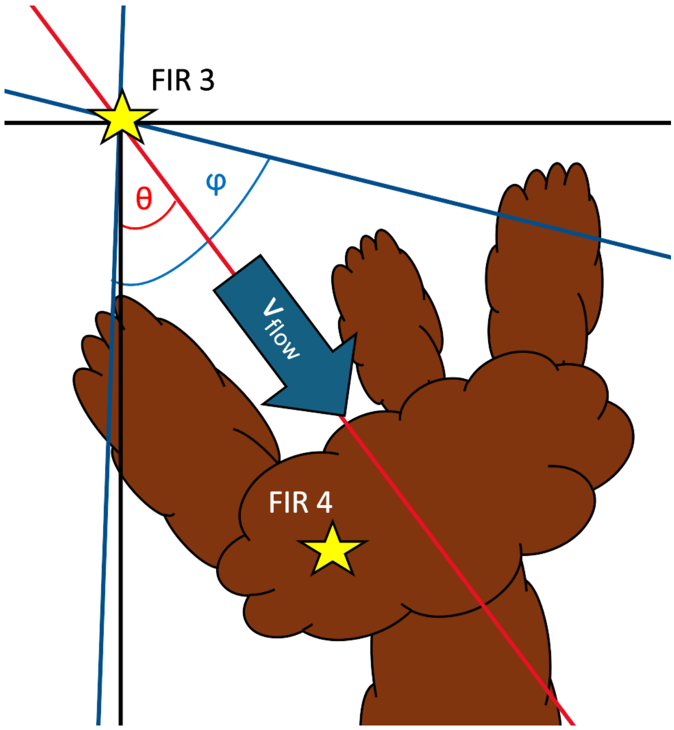

Figure 6.13: Model of the FIR 3 outflow that impacts on the OMC-2 FIR 4 trident structure. The calculated model parameters are the position angle of $\theta = 53°$ (red), the opening angle of $\phi = 78°$ (blue) and the flow velocity of $v_{\rm flow} = 4.5\,{\rm km\,s^{-1}}$. The outflow direction is denoted by the middle red line, while the opening angle boundaries are seen as the outer blue lines. The position of the FIR 3 and FIR 4 protostars are denoted as yellow stars.

All these evidences can be also seen in the data used in this project. The emission of CO(2-1) in Fig. 6.11 shows that the southeast lobe is shorter than the northwest lobe. In addition, the shock tracers in Fig. 6.9 are distributed on the edges of the FIR 4 clump and the CO(2-1) distribution.

To visualize that the FIR 3 outflow might have triggered the star formation in the FIR 4 clump, we created a model of the outflow (see Fig. 6.13). The model assumes a bipolar conic shape (hourglass) with a constant flow velocity along it. This means that the three parameters we have to model are the position angle (outflow direction), the opening angle w.r.t. the plane of the sky, and the flow velocity. We determined the position angle θ by finding the centroids of the blueshifted or redshifted lobe and then applying the following formula:

$$\theta = \arctan\left(\frac{x_{\text{blue/red}} - x_0}{y_{\text{blue/red}} - y_0}\right), \tag{6.8}$$

where $(x_{\text{blue/red}}, y_{\text{blue/red}})$ are the coordinates of the blue or red lobe peak and (x_0, y_0) are the coordinates of the central source (outflow origin). Using the FIR 3 position as the central source of origin and the centroids of the blue lobe as the position of the outflow direction, we determined that the position angle is $\theta \approx 53°$. The position angle (0°) starts in the north-south configuration and increases in the counterclockwise direction. We obtain the opening angle ϕ using the following formula:

$$\phi = 2 \cdot \arctan\left(\frac{w}{2r}\right), \tag{6.9}$$

where r is the projected length of the outflow axis and w the width of the lobe at its widest point. We calculated both quantities in pixel lengths and then used them to calculate the opening angle, which yielded a result of $\phi \approx 78°$. Lastly, we define the flow velocity in two ways:

$$\begin{aligned} v_{\text{flow}} &= \frac{v_{\text{blue}}^{max} - v_{\text{sys}}}{\cos(\frac{\phi}{2} + i)} \\ v_{\text{flow}} &= \frac{v_{\text{red}}^{max} - v_{\text{sys}}}{\cos(\frac{\phi}{2} - i)}, \end{aligned} \tag{6.10}$$

where $v_{\text{blue}}^{max}, v_{\text{red}}^{max}$ are the maximum blushifted and redshifted velocity, ϕ is the opening angle and i is the inclination w.r.t. the plane of the sky. We chose the maximum blushifted and redshifted velocities because they represent the fastest moving gas along the outflow axis and are minimally affected by projection effects or interaction with the ambient medium. We determined the maximum blueshifted and redshifted velocities by searching for the maximum intensity in the blueshifted and redshifted FITS cube. The channel with the according maxima corresponds to the velocities $v_{\text{blue}}^{max} = 7.8\,\text{km}\,\text{s}^{-1}$ and $v_{\text{red}}^{max} = 13.2\,\text{km}\,\text{s}^{-1}$. Since the flow velocity and angle of inclination are unknown, we used both equations to retrieve these quantities. We determined that the flow velocity is $v_{\text{flow}} \approx 4.5\,\text{km}\,\text{s}^{-1}$, while the angle of inclination is $i \approx 105°$. This flow velocity represents the main outflow component, but not the high velocity jet. In both the blueshifted or redshifted spectra, we could not see the high velocity component of the jet. We need higher-resolution and more sensitive CO(2-1) observations to determine the jet.

We plotted the final outflow model on the OMC-2 FIR 4 map with all molecular contours (see Fig. 6.14). The outflow direction goes through the FIR 4 clump, and the opening angle covers the whole bipolar lobes and the clump itself. Furthermore, the shock tracers lie on the edges of the CO(2-1) lobe and the dense gas, indicating the interaction of the modeled outflow with FIR 4.

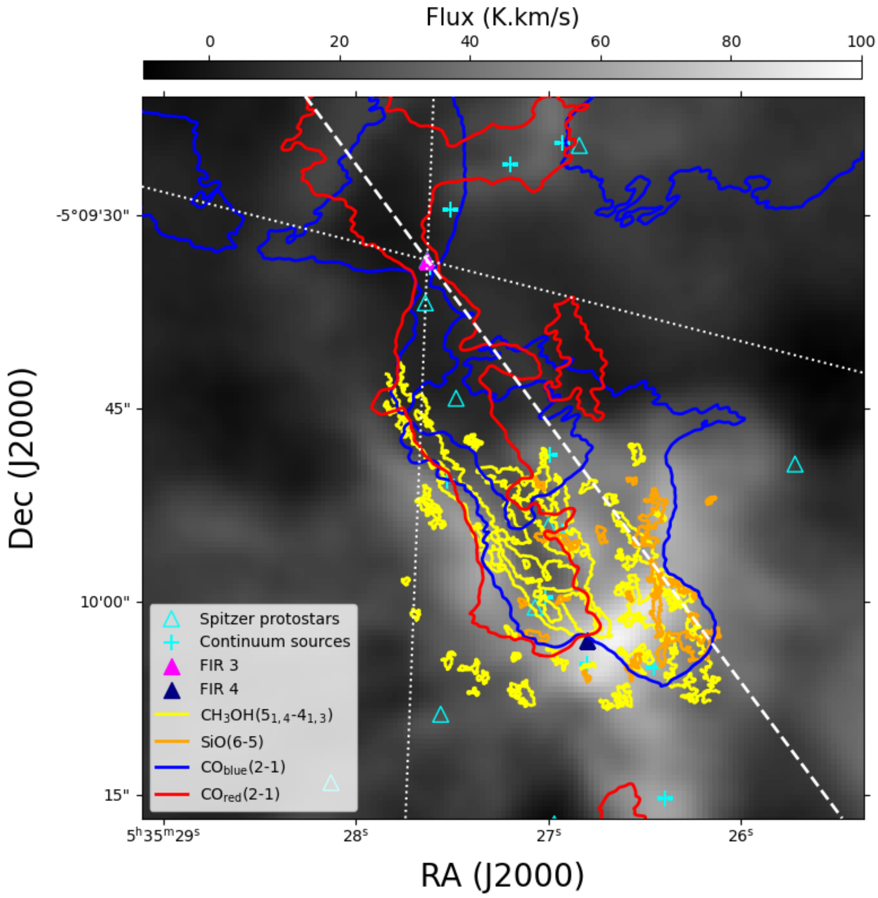

Figure 6.14: Molecular outflow model with position angle of 53°, opening angle of 78° and flow velocity of 4.5 km s^{-1}. The outflow direction is denoted by the white dashed line, while the opening angle boundaries are seen as the white dotted lines. Molecular emission for CO(2-1) blueshifted (blue), CO(2-1) redshifted (red), $CH_3OH(5_{1,4} - 4_{1,3})$ (yellow) and SiO(6-5) (orange) are seen as contours. For reference, the positions of FIR 4 (navy blue triangle), FIR 3 (magenta triangle) (Peterson & Megeath 2008) and both Spitzer protostars (cyan triangles; Megeath et al. (2012); Furlan et al. (2016)) plus continuum sources (cyan crosses; Teixeira et al. (2016); Kainulainen et al. (2017)) are shown.

This plot proves that the schematic overwiev in Fig. 6.12 can be reproduced with interferometric data.

A direct measure of the FIR 3 outflow impact on the FIR 4 clump can be described by the Mach number of the collision. We calculated this Mach number by the ratio of the flow velocity ratio to the local thermal sound speed of H_2 at the edge of the cloud, which resulted in a value of $\mathcal{M}_{\text{collision}} \approx 14$. A Mach number of 14 indicates that the FIR 3 outflow is highly supersonic with respect to the local thermal sound speed in the FIR 4 clump. This implies the presence of strong shocks that are capable of compressing the gas and potentially triggering star formation (Shimajiri et al. 2008; Sato et al. 2023). The high Mach number thus provides a quantitative basis for interpreting the outflow as a driving mechanism for the observed structure and kinematics in the region, as well as for the presence of shock tracers such as $CH_3OH(5_{1,4} - 4_{1,3})$ and SiO(6-5).

7 Summary

7.1 Conclusions

In this project, we used the ALminer toolkit (Ahmadi & Hacar 2023) to explore the molecular content of the OMC-2 region and extract the largest database of ALMA observations from this region (see Sect. 5.1 & 5.2). In particular, our main objective was to explore the gas kinematics of dense tracers such as N_2H^+, while the secondary objective was to characterize OMC-2 with other tracers such as the dust continuum, shock (CH_3OH & SiO) and outflow tracers (e.g. CO). We combined the data of the two chosen N_2H^+(1-0) projects (see Tab. 5.1) and produced a high angular resolution (1.8″) image of OMC-2 FIR 4 thanks to the retrieved Fontani et al. (2020) project while preserving the high sensitivity of the lower resolution image of Hacar et al. (2018) (see Sect. 5.3 & 5.4). We then investigated the dense gas substructure and kinematics in the OMC-2 FIR 4 region using multiple ALMA observations, as well as the shock and outflow components. The results of this project are summarized as follows:

- The resulting dense gas structure (see Fig. 6.2) shows multiple fibers (trident structure) that are connected through the central FIR 4 hub (see Sect. 6.1)
- Our kinematic analysis shows that more or less half of the gas is subsonic (48.9%), while the other half is transonic (35. 0%) and subsonic (16. 1%) (see Tab. 6.1). The Mach numbers we derive in OMC-2 FIR 4 range from 0.3 to 4.3 and do not correlate with high-velocity structures (see Fig. 6.4), such as the FIR 3 outflow (Osorio et al. 2017) or the VLA 15 jet (Chahine et al. 2022) (see Sect. 6.3.1).
- The column densities we derive in OMC-2 FIR 4 correlate with the N_2H^+ dense gas distribution (see Fig. 6.5), where the column densities range from $3 \times 10^{21}\,\mathrm{cm}^{-2}$ to $2 \times 10^{23}\,\mathrm{cm}^{-2}$ (see Sect. 6.3.2).
- The dust continuum map (Fontani et al. 2020) (see Fig. 6.8) traced most of the Spitzer protostars (Furlan et al. 2016) and the bulk distribution of our N_2H^+ dense gas component (see Sect. 6.4).
- The shock tracer $CH_3OH(5_{1,4}-4_{1,3})$ (Chahine et al. 2022) revealed that there is a correlation between the position of the FIR 4 clump cavities and the peak emission (see Fig. 6.9), while the SiO(6-5) emission coincides with the distribution of the VLA 15 jet (see Sect. 6.5).
- The main blue-shifted and red-shifted CO(2-1) emission (Sato et al. 2023) traces the bipolar molecular outflow from FIR 3 (see Fig. 6.11), where the southern outflow impacts the FIR 4 clump (see Sect. 6.6).

- We created a FIR 3 molecular outflow model with a position angle of 53°, opening angle of 78°, and flow velocity of $4.5\,\mathrm{km\,s^{-1}}$ (see Fig. 6.14). Our model and the derived collisional Mach number of 14 provide a quantitative basis for interpreting the outflow as a driving mechanism for the observed structure and kinematics in OMC-2 FIR 4. This implies the presence of strong shocks that are capable of compressing the gas and potentially triggering star formation (Shimajiri et al. 2008) (see Sect. 6.7).

7.2 Outlook

Future investigations of OMC-2 FIR 4 can greatly benefit from incorporating a broader set of molecular tracers, including additional dense gas, shock, and temperature-sensitive lines. High-resolution imaging and polarization measurements could clarify the internal dynamics, fragmentation, and role of magnetic fields. Furthermore, radiative transfer and chemical modeling would help disentangle the observed kinematic complexity, especially in light of the apparent departure from a simple gravitational free-fall scenario. Expanding the analysis to include evolutionary comparisons with neighboring sources like FIR 3 and FIR 5 may also contextualize the triggering and progression of star formation in this active region.

Although this study has focused on OMC-2 FIR 4, extending the analysis to the entire OMC-2 region offers significant scientific value. Comparing the physical and chemical conditions of other dense cores such as FIR 1 and FIR 6 could help distinguish between localized versus global star formation triggers. Moreover, studying the kinematic structure along the filamentary spine, the variation in chemical tracers, and the influence of magnetic fields would offer a comprehensive view of how feedback, gravity, and turbulence shape star formation in filamentary molecular clouds.

Bibliography

Adams, J. D., Herter, T. L., Osorio, M., et al. 2012, , 749, L24

Ahmadi, A. & Hacar, A. 2023, ALminer: ALMA archive mining and visualization toolkit, Astrophysics Source Code Library, record ascl:2306.025

Allen, L., Megeath, S. T., Gutermuth, R., et al. 2007, in Protostars and Planets V, ed. B. Reipurth, D. Jewitt, & K. Keil, 361

André, P., Di Francesco, J., Ward-Thompson, D., et al. 2014, in Protostars and Planets VI, ed. H. Beuther, R. S. Klessen, C. P. Dullemond, & T. Henning, 27–51

André, P., Men'shchikov, A., Bontemps, S., et al. 2010, , 518, L102

Andre, P., Ward-Thompson, D., & Barsony, M. 1993, , 406, 122

Avery, L. W. & Chiao, M. 1996, , 463, 642

Bachiller, R., Pérez Gutiérrez, M., Kumar, M. S. N., & Tafalla, M. 2001, , 372, 899

Bally, J., Langer, W. D., Stark, A. A., & Wilson, R. W. 1987, , 312, L45

Batria, W., Wilson, T. L., Bastien, P., & Ruf, K. 1983, , 128, 279

Bergin, E. A. & Tafalla, M. 2007, , 45, 339

Bjerkeli, P., Liseau, R., Nisini, B., et al. 2013, , 552, L8

Bonanomi, F., Hacar, A., Socci, A., Petry, D., & Suri, S. 2024, , 688, A30

Bouvier, M., López-Sepulcre, A., Ceccarelli, C., et al. 2021, , 653, A117

Briggs, D. S. 1995, in American Astronomical Society Meeting Abstracts, Vol. 187, American Astronomical Society Meeting Abstracts, 112.02

CASA Team, Bean, B., Bhatnagar, S., et al. 2022, , 134, 114501

Caselli, P., Benson, P. J., Myers, P. C., & Tafalla, M. 2002, , 572, 238

Chahine, L., López-Sepulcre, A., Podio, L., et al. 2022, , 667, A6

Chen, H., Myers, P. C., Ladd, E. F., & Wood, D. O. S. 1995, , 445, 377

Chen, J. L., Zhang, J. S., Ge, J. X., et al. 2025, arXiv e-prints, arXiv:2505.23221

Chini, R., Reipurth, B., Sievers, A., et al. 1997a, , 325, 542

Chini, R., Reipurth, B., Ward-Thompson, D., et al. 1997b, , 474, L135

Collaboration, T. A., Price-Whelan, A. M., Lim, P. L., et al. 2022, The Astrophysical Journal, 935, 167

Cornwell, T. J., Holdaway, M. A., & Uson, J. M. 1993, , 271, 697

Cortes, P., Vlahakis, C., Hales, A., et al. 2023, ALMA Cycle 10 Technical Handbook

Cotton, W. D. 2017, , 129, 094501

Coutens, A., Rawlings, J. M. C., Viti, S., & Williams, D. A. 2017, , 467, 737

Crimier, N., Ceccarelli, C., Alonso-Albi, T., et al. 2010, , 516, A102

Crimier, N., Ceccarelli, C., Lefloch, B., & Faure, A. 2009, , 506, 1229

Davis, M. & Peebles, P. J. E. 1983, , 21, 109

Dhabal, A., Mundy, L. G., Rizzo, M. J., Storm, S., & Teuben, P. 2018, , 853, 169

Dirienzo, W. J., Brogan, C., Indebetouw, R., et al. 2015, , 150, 159

Dunham, M. M., Stutz, A. M., Allen, L. E., et al. 2014, in Protostars and Planets VI, ed. H. Beuther, R. S. Klessen, C. P. Dullemond, & T. Henning, 195–218

Dutrey, A., Duvert, G., Castets, A., et al. 1993, , 270, 468

Fernández-López, M., Arce, H. G., Looney, L., et al. 2014, , 790, L19

Fontani, F., Quaia, G., Ceccarelli, C., et al. 2020, , 493, 3412

Friesen, R. 2019, , 51, 441

Friesen, R. K., Pineda, J. E., co-PIs, et al. 2017, , 843, 63

Furlan, E., Fischer, W. J., Ali, B., et al. 2016, , 224, 5

Gatley, I., Becklin, E. E., Mattews, K., et al. 1974, , 191, L121

Gómez-Ruiz, A. I., Gusdorf, A., Leurini, S., et al. 2019, , 629, A77

Hacar, A., Alves, J., Tafalla, M., & Goicoechea, J. R. 2017, , 602, L2

Hacar, A., Bosman, A. D., & van Dishoeck, E. F. 2020, , 635, A4

Hacar, A. & Tafalla, M. 2011, , 533, A34

Hacar, A., Tafalla, M., Forbrich, J., et al. 2018, , 610, A77

Hacar, A., Tafalla, M., Kauffmann, J., & Kovács, A. 2013, , 554, A55

Harris, C. R., Millman, K. J., van der Walt, S. J., et al. 2020, Nature, 585, 357

Hoemann, E., Socci, A., Heigl, S., Burkert, A., & Hacar, A. 2024, , 532, L42

Högbom, J. A. 1974, , 15, 417

Hunter, J. D. 2007, Computing in Science & Engineering, 9, 90

Ishihara, K., Sanhueza, P., Nakamura, F., et al. 2024, , 974, 95

Johnstone, D. & Bally, J. 1999, , 510, L49

Juárez, C., Liu, H. B., Girart, J. M., et al. 2019, , 621, A140

Kainulainen, J., Stutz, A. M., Stanke, T., et al. 2017, , 600, A141

Kauffmann, J., Pillai, T., & Goldsmith, P. F. 2013, , 779, 185

Kauffmann, J., Pillai, T., Zhang, Q., et al. 2017, , 603, A89

Könyves, V., André, P., Men'shchikov, A., et al. 2010, , 518, L106

Li, S., Frank, A., & Blackman, E. G. 2014, , 444, 2884

Lis, D. C., Serabyn, E., Keene, J., et al. 1998, , 509, 299

Lombardi, M., Bouy, H., Alves, J., & Lada, C. J. 2014, , 566, A45

Mann, R. K., Di Francesco, J., Johnstone, D., et al. 2014, , 784, 82

Martin-Pintado, J., Rodriguez-Franco, A., & Bachiller, R. 1990, , 357, L49

McMullin, J. P., Waters, B., Schiebel, D., Young, W., & Golap, K. 2007, in Astronomical Society of the Pacific Conference Series, Vol. 376, Astronomical Data Analysis Software and Systems XVI, ed. R. A. Shaw, F. Hill, & D. J. Bell, 127

Megeath, S. T., Gutermuth, R., Muzerolle, J., et al. 2012, , 144, 192

Megeath, T., Yang, Y.-L., Anglada, G., et al. 2024, HEFE: High Angular Resolution observations of Stellar Emergence in Filamentary Environments, JWST Proposal. Cycle 3, ID. #5804

Menten, K. M., Reid, M. J., Forbrich, J., & Brunthaler, A. 2007, , 474, 515

Mezger, P. G., Wink, J. E., & Zylka, R. 1990, , 228, 95

Myers, P. C. & Benson, P. J. 1983, , 266, 309

Nielbock, M., Chini, R., & Müller, S. A. H. 2003, , 408, 245

Nyquist, H. 1928, Transactions of the American Institute of Electrical Engineers, 47, 617

O'Dell, C. R., Muench, A., Smith, N., & Zapata, L. 2008, in Handbook of Star Forming Regions, Volume I, ed. B. Reipurth, Vol. 4, 544

Osorio, M., Díaz-Rodríguez, A. K., Anglada, G., et al. 2017, , 840, 36

Padovani, M., Marcowith, A., Galli, D., Hunt, L. K., & Fontani, F. 2021, , 649, A149

pandas development team, T. 2020, pandas-dev/pandas: Pandas

Peñaloza, C. H., Clark, P. C., Glover, S. C. O., Shetty, R., & Klessen, R. S. 2017, , 465, 2277

Peterson, D. E. & Megeath, S. T. 2008, in Handbook of Star Forming Regions, Volume I, ed. B. Reipurth, Vol. 4, 590

Pety, J., Guzmán, V. V., Orkisz, J. H., et al. 2017, , 599, A98

Pety, J., Schinnerer, E., Leroy, A. K., et al. 2013, , 779, 43

Plunkett, A., Hacar, A., Moser-Fischer, L., et al. 2023, , 135, 034501

Polychroni, D., Schisano, E., Elia, D., et al. 2013, , 777, L33

Rau, U. & Cornwell, T. J. 2011, , 532, A71

Reipurth, B., Rodríguez, L. F., & Chini, R. 1999, , 118, 983

Rojas-García, O. S., Gómez-Ruiz, A. I., Palau, A., et al. 2022, , 262, 13

Sato, A., Takahashi, S., Ishii, S., et al. 2023, , 944, 92

Schneider, N., Csengeri, T., Hennemann, M., et al. 2012, , 540, L11

Schuller, F., André, P., Shimajiri, Y., et al. 2021, , 651, A36

Shimajiri, Y., Kawabe, R., Takakuwa, S., et al. 2011, , 63, 105

Shimajiri, Y., Takahashi, S., Takakuwa, S., Saito, M., & Kawabe, R. 2008, , 683, 255

Shu, F. H., Ruden, S. P., Lada, C. J., & Lizano, S. 1991, , 370, L31

Socci, A., Hacar, A., Bonanomi, F., Tafalla, M., & Suri, S. 2024, , 690, A376

Soker, N., Bublitz, J., & Kastner, J. H. 2022, , 928, 159

Stutz, A. M., Tobin, J. J., Stanke, T., et al. 2013, , 767, 36

Tafalla, M., Santiago-García, J., Hacar, A., & Bachiller, R. 2010, , 522, A91

Taylor, M. B. 2005, in Astronomical Society of the Pacific Conference Series, Vol. 347, Astronomical Data Analysis Software and Systems XIV, ed. P. Shopbell, M. Britton, & R. Ebert, 29

Teixeira, P. S., Takahashi, S., Zapata, L. A., & Ho, P. T. P. 2016, , 587, A47

Thronson, H. A., J., Harper, D. A., Keene, J., et al. 1978, , 83, 492

Tobin, J. J., Sheehan, P. D., Reynolds, N., et al. 2020, , 905, 162

Tsujimoto, M., Koyama, K., Kobayashi, N., et al. 2003, , 125, 1537

van Terwisga, S. E., Hacar, A., & van Dishoeck, E. F. 2019, , 628, A85

Virtanen, P., Gommers, R., Oliphant, T. E., et al. 2020, Nature Methods, 17, 261

Williams, J. 2021, Introduction to the Interstellar Medium (Cambridge University Press)

Yokogawa, S., Kitamura, Y., Momose, M., & Kawabe, R. 2003, , 595, 266